

RESEARCH ARTICLE SUMMARY

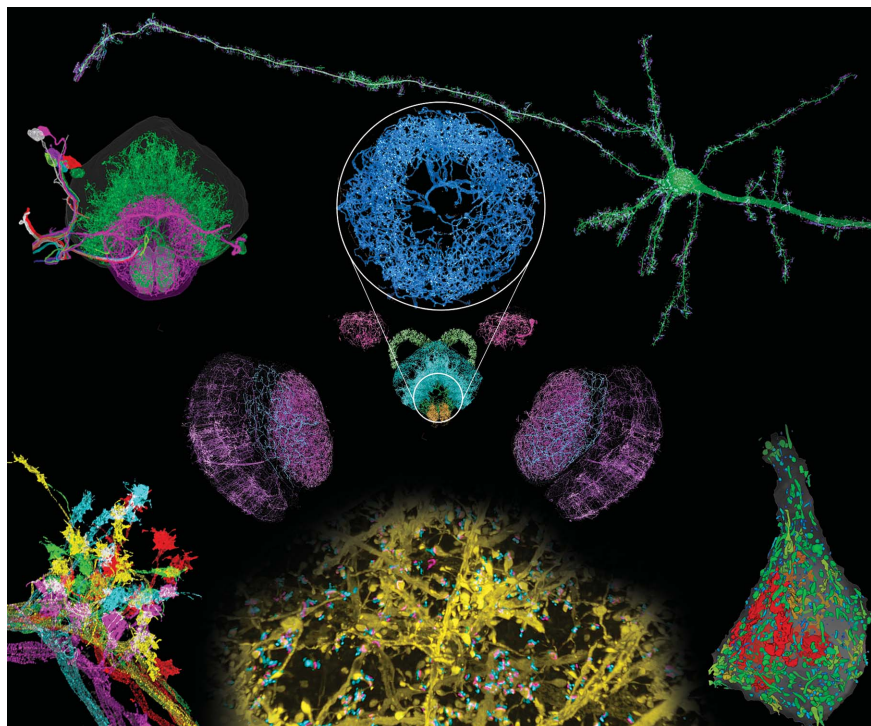
IMAGING TECHNIQUES

Cortical column and whole-brain imaging with molecular contrast and nanoscale resolution

Ruixuan Gao*, Shoh M. Asano*, Srigokul Upadhyayula*, Igor Pisarev, Daniel E. Milkie, Tsung-Li Liu, Ved Singh, Austin Graves, Grace H. Huynh, Yongxin Zhao, John Bogovic, Jennifer Colonell, Carolyn M. Ott, Christopher Zugates, Susan Tappan, Alfredo Rodriguez, Kishore R. Mosaliganti, Shu-Hsien Sheu, H. Amalia Pasolli, Song Pang, C. Shan Xu, Sean G. Megason, Harald Hess, Jennifer Lippincott-Schwartz, Adam Hantman, Gerald M. Rubin, Tom Kirchhausen, Stephan Saalfeld, Yoshinori Aso, Edward S. Boyden†, Eric Betzig†

INTRODUCTION: Neural circuits across the brain are composed of structures spanning seven orders of magnitude in size that are assembled from thousands of distinct protein types. Electron microscopy has imaged densely labeled brain tissue at nanometer-level resolution over near-millimeter-level dimensions but lacks the contrast to distinguish specific pro-

teins and the speed to readily image multiple specimens. Conversely, confocal fluorescence microscopy offers molecular contrast but has insufficient resolution for dense neural tracing or the precise localization of specific molecular players within submicrometer-sized structures. Last, superresolution fluorescence microscopy bleaches fluorophores too quickly for large



Nanoscale brain-wide optical imaging. ExLLSM images neural structures with molecular contrast over millimeter-scale volumes, including (clockwise from top right) mouse pyramidal neurons and their processes; organelle morphologies in somata; dendritic spines and synaptic proteins across the cortex; stereotypy of projection neuron boutons in *Drosophila*; projection neurons traced to the central complex; and (center) dopaminergic neurons across the brain, including the ellipsoid body (circular inset).

volume imaging and also lacks the speed for effective brain-wide or cortex-wide imaging of multiple specimens.

RATIONALE: We combined two imaging technologies to address these issues. Expansion microscopy (ExM) creates an expanded, optically clear phantom of a fluorescent specimen that retains its original relative distribution of fluorescent tags. Lattice light-sheet microscopy (LLSM)

then images this phantom in three dimensions with minimal photobleaching at speeds sufficient to image the entire *Drosophila* brain or across the width of the mouse cortex in ~2 to 3 days,

with multiple markers at an effective resolution of ~60 by 60 by 90 nm for 4 \times expansion.

RESULTS: We applied expansion/LLSM (ExLLSM) to study a variety of subcellular structures in the brain. In the mouse cortex, we quantified the volume of organelles, measured morphological parameters of ~1500 dendritic spines, determined the variation of distances between pre- and postsynaptic proteins, observed large differences in postsynaptic expression at adjacent pyramidal neurons, and studied both the azimuthal asymmetry and layer-specific longitudinal variation of axonal myelination. In *Drosophila*, we traced the axonal branches of olfactory projection neurons across one hemisphere and studied the stereotypy of their boutons at the calyx and lateral horn across five animals. We also imaged all dopaminergic neurons (DANs) across the brain of another specimen, visualized DAN morphologies in all major brain regions, and traced a cluster of eight DANs to their termini to determine their respective cell types. In the same specimen, we also determined the number of presynaptic active zones (AZs) across the brain and the local density of all AZs and DAN-associated AZs in each brain region.

CONCLUSION: With its high speed, nanometric resolution, and ability to leverage genetically targeted, cell type-specific, and protein-specific fluorescence labeling, ExLLSM fills a valuable niche between the high throughput of conventional optical pipelines of neural anatomy and the ultrahigh resolution of corresponding EM pipelines. Assuming the development of fully validated, brain-wide isotropic expansion at 10 \times or beyond and sufficiently dense labeling, ExLLSM may enable brainwide comparisons of even densely innervated neural circuits across multiple specimens with protein-specific contrast at 25-nm resolution or better. ■

The list of author affiliations can be found in the full article online.

*These authors contributed equally to this work.

†Corresponding author. Email: esb@mit.edu (E.S.B.); betzige@janelia.hhmi.org (E.B.)

Cite this article as R. Gao et al., *Science* 363, eaau8302 (2019). DOI: 10.1126/science.aau8302

RESEARCH ARTICLE

IMAGING TECHNIQUES

Cortical column and whole-brain imaging with molecular contrast and nanoscale resolution

Ruixuan Gao^{1,2,3*}, Shoh M. Asano^{1,2*†}, Srigokul Upadhyayula^{3,4,5,6*}, Igor Pisarev³, Daniel E. Milkie³, Tsung-Li Liu^{3‡}, Ved Singh^{3§}, Austin Graves^{3¶}, Grace H. Huynh^{1#}, Yongxin Zhao^{1**}, John Bogovic³, Jennifer Colonell³, Carolyn M. Ott³, Christopher Zugates⁷, Susan Tappan⁸, Alfredo Rodriguez⁸, Kishore R. Mosaliganti⁹, Shu-Hsien Sheu³, H. Amalia Pasolli³, Song Pang³, C. Shan Xu³, Sean G. Megason⁹, Harald Hess³, Jennifer Lippincott-Schwartz³, Adam Hantman³, Gerald M. Rubin³, Tom Kirchhausen^{3,4,5,6}, Stephan Saalfeld³, Yoshinori Aso³, Edward S. Boyden^{1,2,10,11,12,13††}, Eric Betzig^{3,14,15,16,17,18††}

Optical and electron microscopy have made tremendous inroads toward understanding the complexity of the brain. However, optical microscopy offers insufficient resolution to reveal subcellular details, and electron microscopy lacks the throughput and molecular contrast to visualize specific molecular constituents over millimeter-scale or larger dimensions. We combined expansion microscopy and lattice light-sheet microscopy to image the nanoscale spatial relationships between proteins across the thickness of the mouse cortex or the entire *Drosophila* brain. These included synaptic proteins at dendritic spines, myelination along axons, and presynaptic densities at dopaminergic neurons in every fly brain region. The technology should enable statistically rich, large-scale studies of neural development, sexual dimorphism, degree of stereotypy, and structural correlations to behavior or neural activity, all with molecular contrast.

The human brain is a 1.5-kg organ that, despite its small size, contains more than 80 billion neurons (1) that connect through approximately 7000 synapses each in a network of immense complexity. Neural structures span a size continuum greater than seven orders of magnitude in extent and are composed of more than 10,000 distinct protein types (2) that collectively are essential to build and maintain neural networks. Electron microscopy (EM) can image down to the level of individual ion channels and synaptic vesicles (3) across the ~0.03 mm³ volume of the brain of the fruitfly *Drosophila melanogaster* (4, 5). However, EM creates a grayscale image in which the segmentation of specific subcellular components or the tracing of the complete arborization of specific neurons remains challenging and in which specific proteins can rarely be unambiguously identified. Optical microscopy combined with

immunofluorescence, fluorescent proteins, or fluorescence in situ hybridization (FISH) enables high-sensitivity imaging of specific protein expression patterns in brain tissue (6, 7), brain-wide tracing of sparse neural subsets in flies (8, 9) and mice (10), and in situ identification of specific cell types (11, 12) but has insufficient resolution for dense neural tracing or the precise localization of specific molecular players within critical subcellular structures such as dendritic spines. Diffraction-unlimited superresolution (SR) fluorescence microscopy (13, 14) combines nanoscale resolution with protein-specific contrast but bleaches fluorophores too quickly for large-volume imaging and, like EM, would require months to years to image even a single *D. melanogaster* brain (table S1).

Given the vast array of molecular species that contribute to neural communication through many mechanisms in addition to the synaptic

connections determined by EM connectomics (15), and given that the anatomical circuits for specific tasks can vary substantially between individuals of the same species (16, 17), high-resolution three-dimensional (3D) imaging with molecular specificity of many thousands of brains may be necessary to yield a comprehensive understanding of the genesis of complex behaviors in any organism. Here, we describe a combination of expansion microscopy (ExM) (18, 19), lattice light-sheet microscopy (LLSM) (20), and terabyte-scale image processing and analysis tools (21) that achieves single-molecule sensitivity and ~60- by 60- by 90-nm resolution at volumetric acquisition rates ~700× and 1200× faster than existing high-speed SR (22) and EM (5) methods, respectively, at comparable or higher resolution (table S1). We demonstrate its utility through multicolor imaging of neural subsets and associated proteins across the thickness of the mouse cortex and the entirety of the *Drosophila* brain while quantifying nanoscale parameters, including dendritic spine morphology, myelination patterns, stereotypic variations in boutons of fly projection neurons, and the number of synapses in each fly brain region.

Combining expansion and lattice light-sheet microscopy (ExLLSM)

In protein-retention ExM (proExM) (19), fluorophore-conjugated antibodies (Abs) and/or fluorescent proteins (FPs) that mark the features of interest within a fixed tissue are chemically linked to an infused polyacrylamide/polyacrylate gel. After protease digestion of the tissue, the gel can be expanded in water isotropically, creating an enlarged phantom of the tissue that faithfully retains the tissue's original relative distribution of fluorescent tags (fig. S1 and supplementary note 1). This yields an effective resolution given by the original resolution of the imaging microscope divided by the expansion factor. Another advantage of digestion is that lipids, protein fragments, and other optically inhomogeneous organic components that are not anchored to the gel are sufficiently removed so that the expanded gel has a refractive index nearly indistinguishable from water and therefore can be imaged aberration-free to a postexpansion depth of at least 500 μm (fig. S2) by using conventional water immersion objectives. ProExM has been applied to a range of model animals, including mouse (19), zebrafish (23), and *Drosophila* (24–28). Although up to 20× expansion has been reported (29), at 8× expansion by using an iterated form of

*These authors contributed equally to this work. †Present address: Internal Medicine Research Unit, Pfizer, Cambridge, MA 02139, USA. ‡Present address: Vertex Pharmaceuticals, 3215 Merryfield Row, San Diego, CA 92121, USA. §Present address: Intel, 2501 Northwest 229th Avenue, Hillsboro, OR 97124, USA. ¶Present address: Department of Neuroscience, Johns Hopkins University School of Medicine, Baltimore, MD 21205, USA. #Present address: Microsoft Research Lab, 14820 NE 36th Street, Redmond, WA 98052, USA. **Present address: Department of Biological Sciences, Carnegie Mellon University, Pittsburgh, PA 15143, USA. ††Corresponding author. Email: esb@media.mit.edu (E.S.B.); betzige@janelia.hhmi.org (E.B.).

the N,N-dimethylacrylamide-gel expansion protocol, we observed regions where the expansion superficially appears accurate (fig. S3A) and other regions of clear distortion, such as irregularly shaped somata and nuclei (fig. S3B). High expansion ratios also require exceptionally high fluorescence labeling densities to take advantage of the theoretically achievable resolution and take longer to image. Thus, for this work we chose to focus only on applications (table S2) enabled by 4 \times expansion.

Several challenges emerge when attempting to extend ExM to specimens at the millimeter scale of the fly brain or a mouse cortical column. First, even 4 \times expansion requires effective voxel dimensions of ~30 to 50 nm on each side to match the full resolution potential of ExM, or ~20 trillion voxels/mm³/color. This in turn necessitates imaging at speeds on the order of 100 million voxels/s to complete the acquisition in days rather than weeks or more, as well as an image-processing and -storage pipeline that can handle such high sustained data rates. Second, photobleaching often extinguishes the fluorescence signal from deeper regions of 3D specimens before they can be imaged—a problem that becomes more severe with thicker specimens, longer imaging durations, and/or the higher illumination intensities needed for faster imaging. Last, because ExM resolution is proportional to imaging resolution, the latter should be as high as possible within these other constraints while also striving for near-isotropic resolution, so that neural tracing and quantification of nanoscale structures is not limited by the axis of poorest resolution.

To address these challenges, we turned to LLSM (20), which sweeps an ultrathin sheet of laser light through a specimen and collects the resulting fluorescence from above with a high numerical aperture (NA) objective to image it on a high-speed camera (supplementary note 2). Confinement and propagation of excitation light within the detection focal plane permits parallel acquisition of data at rates of 10 million to 100 million voxels/s at low intensities that minimize photobleaching within the plane and eliminates bleaching in the unilluminated regions above and below. Consequently, we could image large volumes of expanded tissue expressing yellow fluorescent protein (YFP) in a subset of mouse cortical neurons with uniform signal from top to bottom (Fig. 1A, left). By contrast, at a comparable signal in the acquired images, the out-of-focus excitation and high peak power at the multiple foci of a spinning disk confocal microscope (SDCM) photobleached the expanded tissue ~10 \times faster than LLSM (Fig. 1C), rendering deeper regions completely dark (Fig. 1, A and B, center), while the sparse illumination of the SDCM focal array slowed volumetric acquisition by ~7 \times (table S1). Another commercial alternative, Airyscan, efficiently images the fluorescence generated at the excitation focus and uses this information to extend the imaging resolution approximately 1.4 \times beyond the diffraction limit (30, 31). However, Airyscan imaged

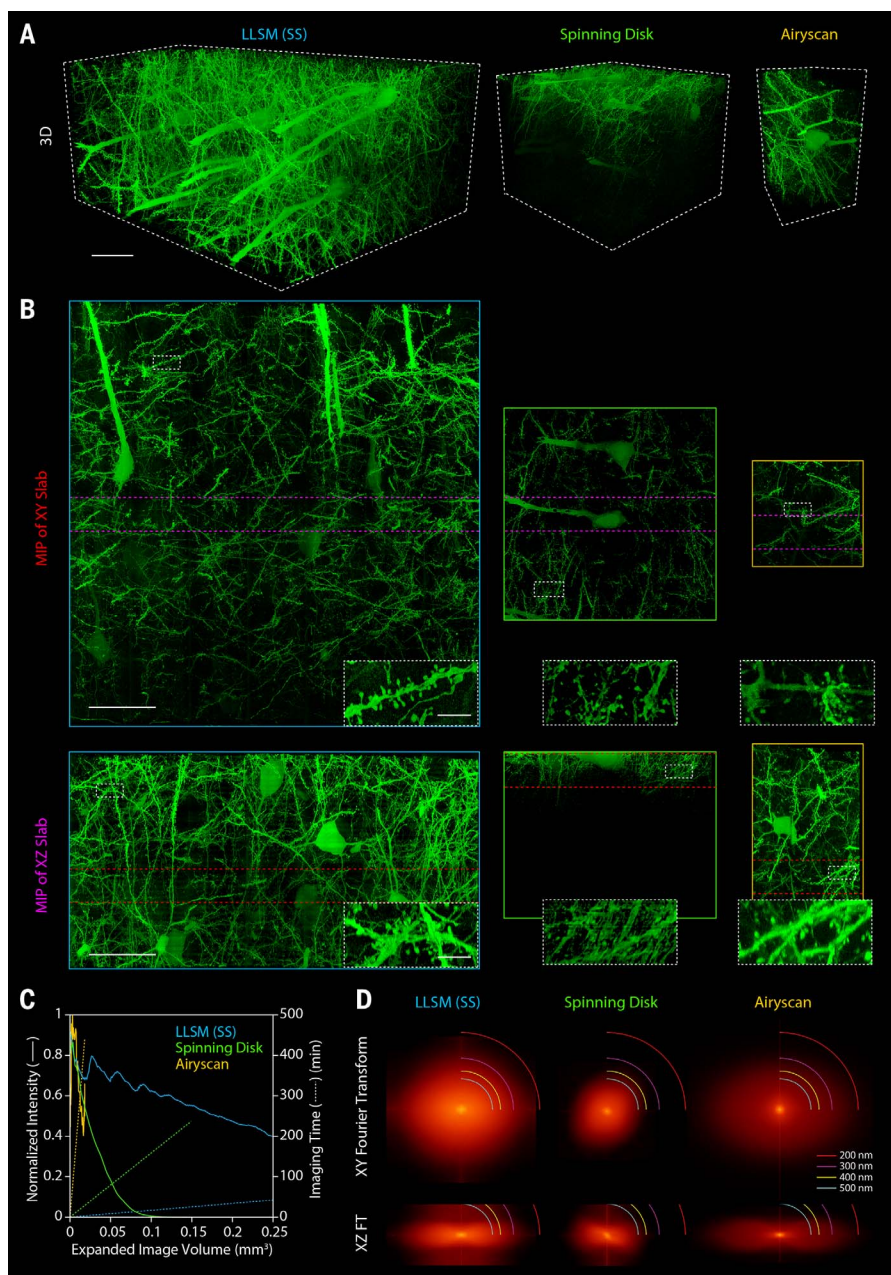


Fig. 1. Comparing modalities to image-expanded mouse brain tissue. (A) 3D rendered volumes at equal magnification of tissue sections from the primary somatosensory cortex of a Thy1-YFP transgenic mouse, expanded ~4 \times by using the protein-retention expansion microscopy (proExM) protocol and imaged by means of (left to right) LLSM in sample scan mode [LLSM (SS), blue]; spinning disk confocal microscopy (Spinning Disk, green); and Airyscan in fast mode (Airyscan, orange). Scale bars, 50 μ m, here and elsewhere given in preexpanded (biological) dimensions. (B) (Top) xy and (bottom) xz maximum intensity projections (MIPs) of 25- μ m-thick slabs cut from the image volumes in (A) at the locations denoted by the red and purple lines in the slabs perpendicular to them, respectively. (Insets) Regions in the white rectangles at higher magnification. Scale bars, 50 μ m, full MIPs; 5 μ m, insets. (C) Comparative imaging and photobleaching rates for the three modalities (table S1). (D) (Top) xy and (bottom) xz spatial frequency content in the same three image volumes as measured from mitochondria-targeted antibody puncta, with different resolution bands as shown (fig. S4).

expanded tissue ~40 \times slower (table S1) and with ~20 \times faster bleaching (Fig. 1C) than LLSM.

LLSM can operate in two modes: objective scan (fig. S4), in which the sample is stationary while the light-sheet and detection objective

move in discrete steps across the image volume, and sample scan (Fig. 1), in which the sample is swept continuously through the light sheet. Sample scan is faster (tables S1) but yields slightly lower y/z resolution (fig. S4) than that of

objective scan because information in the sample scanning direction is slightly blurred by simultaneous image acquisition and sample movement. Of the methods above, Airyscan should in principle achieve the highest lateral (xy) resolution, followed by SDCM (owing to pinhole filtering), and last, the two modes of LLSM. In practice, however, dendritic spines and axons appeared more clearly and faithfully resolved in lateral views with LLSM than with SDCM or even Airyscan (Fig. 1B, top row), a conclusion corroborated by its higher lateral spatial frequency content (Fig. 1D and fig. S4A, top rows) as measured from mitochondria-targeted Ab puncta. Likewise, the thinness of the lattice light sheet contributes to the axial (z) resolution of LLSM (Fig. 1D and fig. S4A, bottom rows) and therefore yielded xz views of spines and axons only slightly poorer than in the lateral plane and substantially sharper than those obtained with SDCM or Airyscan (Fig. 1B, bottom row).

One additional challenge in millimeter-scale ExLLSM involves the processing of multiterabyte data sets. In LLSM, the lateral extent of the light sheet (table S2) is far smaller than an expanded fly brain or cortical column, so the final image volumes had to be computationally stitched together from as many as 25,000 (table S2) tiled subvolumes per color. However, because of systematic sample stage errors and slight swelling or shrinking of expanded samples over many hours, many tiles did not perfectly overlap with their neighbors on all six sides. To address this, we developed an Apache Spark-based high-performance computing pipeline (supplementary note 3 and figs. S5 to S7) that first performed a flat-field correction for each tile to account for intensity variations across the light sheet and then stitched the intensity-corrected tiles together by using an automated and iteratively refined prediction model of tile coordinates. In a separate track, each intensity-corrected tile was deconvolved by using a measured point spread function (PSF) so that when the final set of coordinates for all tiles was available, the deconvolved image volume of the entire specimen could be assembled and visualized (supplementary note 4 and 5) with minimal stitching artifacts.

Quantification of subcellular structures in mouse cortical neurons

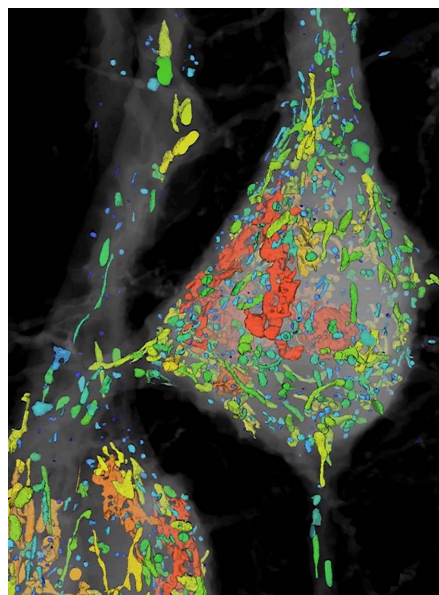
The protein-specific fluorescence contrast of ExLLSM enabled rapid, computationally efficient, and purely automated segmentation and nanoscale quantification of subcellular neural structures over large volumes. For example, dense cytosolic expression of YFP under the *thyl* promoter in mouse pyramidal neurons revealed sharply delineated voids (Movie 1) representing subcellular compartments (Fig. 2A) of various shapes and sizes whose volumes we could quantify accurately (Fig. 2B and supplementary note 4d). Simultaneous immunofluorescence labeling against Tom20 and LAMP1, although comparatively sparse (movie S1), was sufficient to identify the subset of these that

represented mitochondria or lysosomes (Fig. 2C)—in the latter case, the specific subset with LAMP1 that likely represented multivesicular bodies or autolysosomes (supplementary note 6a) (32). As expected, we found that mitochondria were generally both longer and larger in volume than lysosomes (Fig. 2D and table S3). Mitochondria ranged in length from 0.2 to 8.0 μm , which is consistent with EM measurements in the cortex (33) or other regions (34) of the mouse brain, whereas the subset of LAMP1 compartments ranged from 0.1 to ~1.0 μm , which is also consistent with EM (35).

Given this agreement—and the important roles mitochondria play in dendrite development, synapse formation, calcium regulation, and neurodegenerative disease (34, 36, 37)—we extended our analysis across ~100 by 150 by 150 μm of the mouse somatosensory cortex. We classified length, aspect ratio, and volume (Fig. 2E and fig. S8) of 2893 mitochondria and 222 lysosomes across the somata and initial portions (78 μm mean length) of the apical dendrite of five-layer V pyramidal neurons, as well as the initial portions (95 μm mean length) of three descending axon segments. As noted previously in the hippocampus (36), we found that long and high-aspect-ratio mitochondria were far more prevalent in apical dendrites than in axons, with mitochondria longer than 3 μm comprising 6.5% all dendritic mitochondria (~12 per 100 μm of dendrite length) versus 0.7% of all axonal ones. These differences may represent the difficulty in assembling and main-

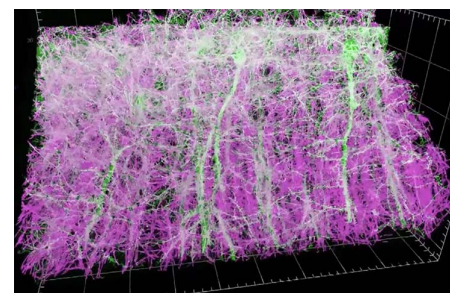
taining large organelles within the narrow confines of the axon, or they may reflect functional differences in the regulation of calcium in axons versus dendrites.

We next turned our attention to the myelination of axons, which is essential for the rapid (38, 39) and energy-efficient (40) propagation of action potentials (APs) and which, when disrupted, can lead to neurodegenerative diseases such as multiple sclerosis (41). The propagation velocity is affected by the g-ratio, the diameter of the axon normalized to the diameter of its surrounding myelin sheath (42). Most EM measurements of the g-ratio come from 2D images of single sections cut transversely to axonal tracts (43–45) and therefore lack information on how the g-ratio might vary along the length of a given axon. To address this, we used ExLLSM to image a 320- by 280- by 60- μm volume in the primary somatosensory cortex of a Thy1-YFP transgenic mouse immunostained against myelin basic protein (MBP) (Fig. 2F and Movie 2). At every longitudinal position z along a given myelinated axon, we measured the local g-ratio at every azimuthal position θ by dividing the radius $r_{\text{axon}}(\theta, z)$ of the axon along the radial vector from the axon center by the radius $r_{\text{myelin}}(\theta, z)$ of the outer edge of the myelin sheath along the same vector (Fig. 2G, fig. S9, and supplementary note 4e). Across one 56- μm -long segment, the mean g-ratio of 0.57 calculated from mean axon and sheath diameters of 0.52 and 0.90 μm , respectively, fell at the lower end of a distribution previously reported in the central nervous system yet was consistent with a theoretical estimate of 0.60 for the ratio that optimizes propagation velocity (42). However, these values do not reflect the substantial variability we observed, with the outer axon-to-outer myelin distance ranging from 0.12 to 0.35 μm (fig. S10) and the local g-ratio ranging from ~0.4 to 0.8 (Fig. 2H and Movie 2). Furthermore, the axon and the sheath were rarely concentric (Fig. 2G), leading to rapid longitudinal changes in capacitance and impedance that may



Movie 1. Organelle analysis of layer V pyramidal neurons in the mouse somatosensory cortex.

Segmentation of cytosolic voids in Thy1-YFP-expressing neurons, quantification of their volumes, and immunostaining-based classification of those voids that represent mitochondria or multivesicular bodies or autolysosomes (Fig. 2, A to E; fig. S8; and movie S1).



Movie 2. Axon myelination and local g-ratio of layer V pyramidal neurons of the mouse primary somatosensory cortex.

Thy1-YFP-expressing neurons and immunostained myelin sheaths across 320 by 280 by 60 μm , with quantification of the local g-ratio on the surface of a specific myelin sheath (Fig. 2, F and G, and figs. S9 and S10).

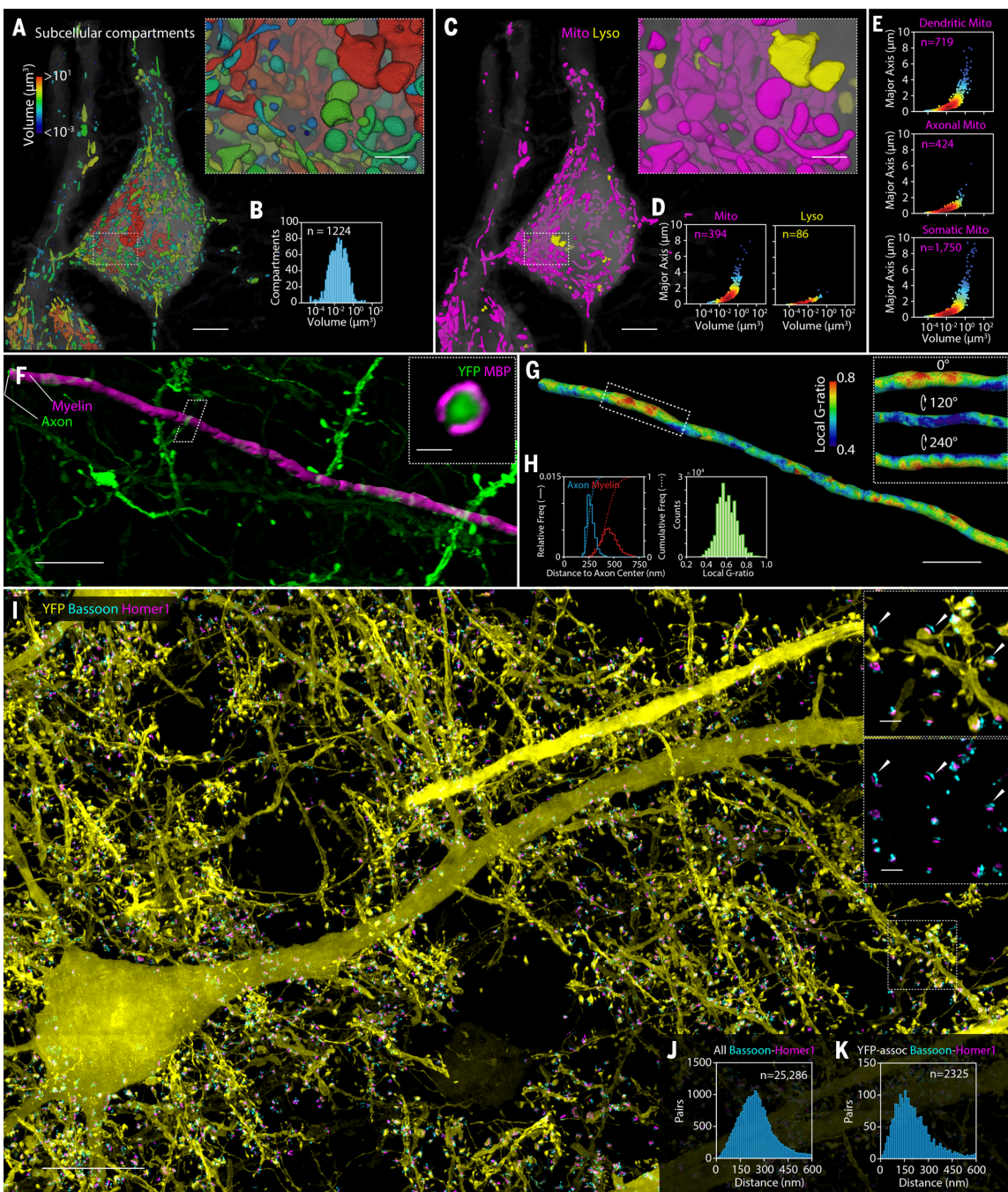


Fig. 2. Nanoscale, protein-specific 3D imaging of subcellular neural structures. (A) Segmented compartments void of cytosolic YFP (gray), color-coded by volume, in portions of the somata and apical dendrites of two layer V pyramidal neurons from the somatosensory cortex of a Thy1-YFP mouse (Movie 1). Scale bars, 5 μm and (inset) 1 μm . (B) Distribution of the compartment volumes. (C) Same region as (A), with voids identified with immunostaining (movie S1) as either mitochondria (magenta) or multivesicular bodies or autolysosomes (yellow). (D) Scatter plots of the major axis (long axis) length versus volume for the two organelle types. Point colors in (D) and (E) indicate relative data point density (blue, low; red, high). (E) Similar scatter plots for mitochondria only, separated by cellular region (fig. S8). (F) Axon of a layer V pyramidal neuron and its surrounding myelin sheath, from the primary somatosensory cortex of another Thy1-YFP mouse, immunostained against myelin (Movie 2). (Inset) A cross-sectional view through the white parallelogram. Scale bars, 5 μm and (inset) 500 nm. (G) Same region as (F), with the myelin sheath color coded according to the local g-ratio (fig. S10). (Inset) Azimuthal variation in g-ratio in the region within the rectangle. Scale bar, 5 μm . (H) (Left) Distribution of axon radius and myelin outer radius and (right) distribution of g-ratio at all points on the axon in (G). (I) xy MIP of a 9.3- μm -thick slab within a 75- by 100- by 125- μm volume from the primary somatosensory cortex of a Thy1-YFP mouse, immunostained against synaptic proteins Bassoon and Homer1 (Movie 3 and fig. S10). Only YFP-associated Bassoon/Homer1 pairs are shown for clarity. (Inlets) (Top) magnified xy MIP of a 2.2- μm -thick slab from boxed region at right. (Bottom) All Bassoon/Homer1 pairs in the same region. Three pairs are indicated with arrows. Scale bars, 10 μm and (insets) 1 μm . (J) Distribution of distances between paired Bassoon and Homer1 centroids across the entire volume. (K) Distribution when restricted to only those pairs associated with YFP-expressing neurons.

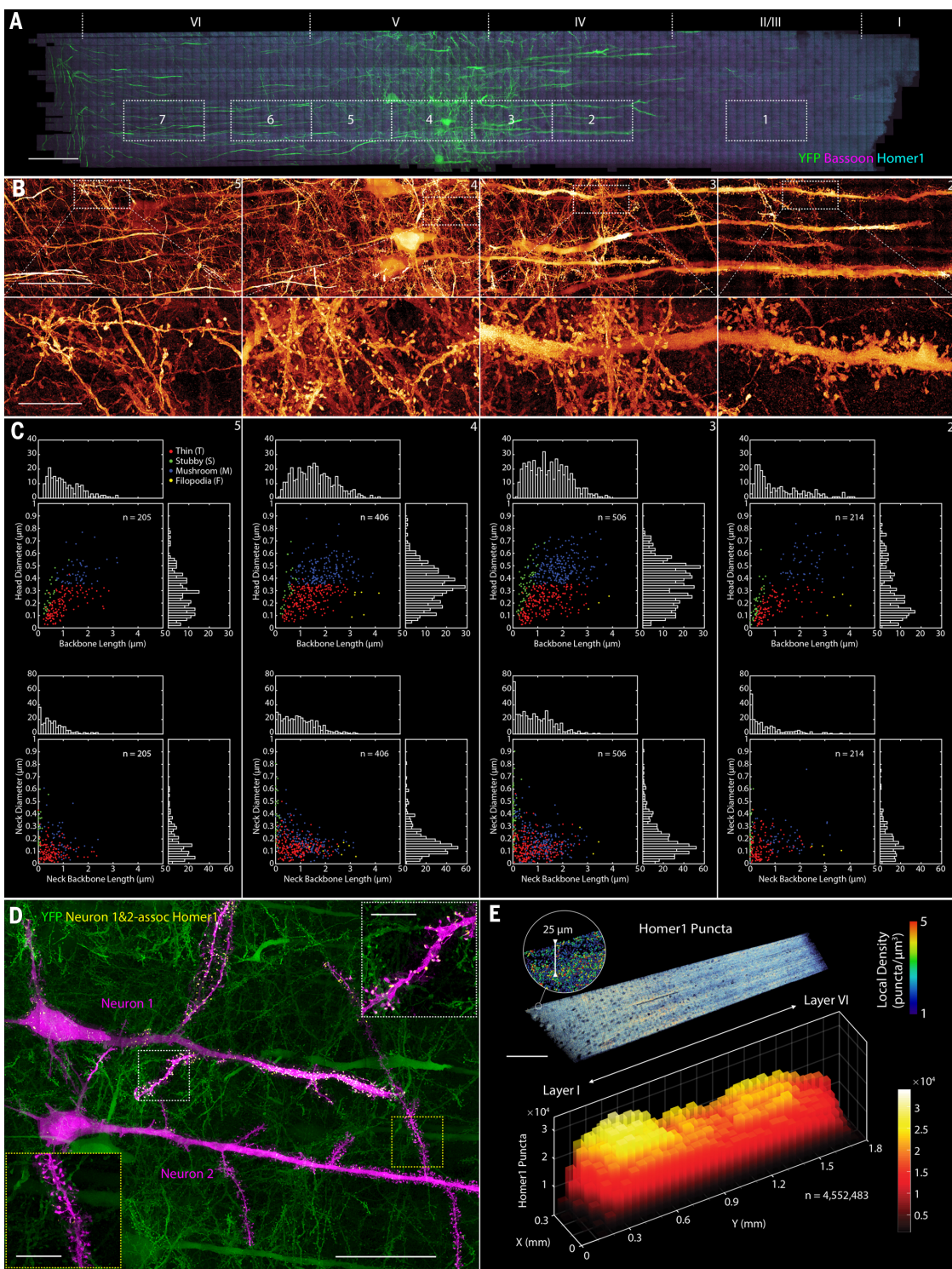


Fig. 3. Characterizing dendritic spine morphologies and postsynaptic Homer1 across the mouse primary somatosensory cortex. (A) Coronal MIP of a 1900- by 280- by 70- μm tissue section spanning the pia to the white matter of the primary somatosensory cortex of a Thy1-YFP mouse (Movie 4), additionally immunostained against Bassoon and Homer1. Boxes denote seven regions for quantitative morphological analysis of dendritic spines. Scale bar, 100 μm . (B) (Top) Magnified MIPs of YFP-expressing neurons in four of the regions from (A), with (bottom) further magnified subregions showing differing spine morphologies. Scale bars, (top) 50 μm and (bottom) 10 μm . (C) Scatter plots and histograms

indicating relationships between (top) spine backbone length and head diameter and (bottom) spine neck length and neck diameter in the four regions from (B) (figs. S13 to S15 and movie S2). (D) Two adjacent layer V pyramidal neurons selected within the volume (magenta), one exhibiting strong Homer1 expression (neuron 1) and the other exhibiting weak expression (neuron 2). (Insets) Homer1 localization or lack thereof at apical dendritic spines (fig. S17). Scale bars, 50 μm and (insets) 10 μm . (E) (Top) MIP of the local density of Homer1 puncta across a ~25- μm -thick coronal slab, and (bottom) the cumulative number of puncta in 50- by 50- by 25- μm subvolumes across the cortex.

influence the speed and efficiency of signal propagation. We subsequently confirmed these observations with EM (fig. S11 and supplementary note 2h).

ExLLSM is also well suited to study the nanoscale organization of synaptic proteins over large tissue volumes. Imaging a 75- by 100- by 125- μm tissue section cut from layer IV/V of the primary somatosensory cortex of a transgenic Thy1-YFP mouse, we identified 25,286 synapses that have closely juxtaposed concentrations of immunolabeled pre- and postsynaptic proteins Bassoon and Homer1 (fig. S12A), 2325 of which had Homer1 localized at YFP-labeled dendritic spines (Fig. 2I and Movie 3). These tended to form nested caps, with major axis lengths of 856 ± 181 nm and 531 ± 97 nm for Bassoon and Homer1, respectively [median \pm median absolute deviation (MAD)] (fig. S12, B and C). The Homer1 distribution was consistent with SR measurements in dissociated hippocampal neurons (DHN) (46), but our Bassoon values were slightly larger. The centroid-to-centroid distance we measured between Bassoon/Homer1 pairs was 243 ± 69 nm for all pairs within the volume (Fig. 2J) and 185 ± 70 nm for those associated with YFP-filled spines (Fig. 2K). The difference between these values suggests that mature glutamatergic synapses of layer V pyramidal neurons, which are the ones expressing YFP, are narrower than other types across the primary somatosensory cortex. The difference between these values and previous SR measurements of 150 ± 20 nm in the ventral orbital cortex ($n = 252$ Bassoon/Homer1 pairs) (47), 165 ± 9 nm in DHN ($n = 43$ pairs) (46), and 179 ± 42 nm in the middle of the primary somatosensory cortex ($n = 159$ pairs) (29) may reflect natural variations in different brain regions (29) or a systematic bias in these earlier studies arising by measuring the distance between 1D Gaussian fits to the Bassoon/Homer1 distributions in a manually selected slice through the heart of each synapse, versus our approach of calculating the distance between the 3D centroids calculated across the complete distributions.

Somatosensory cortex–spanning measurement of dendritic spines and excitatory synapses

The combination of fast imaging (table S1) and targeted sparse labeling enables ExLLSM-based quantification of nanoscale neural structures to be extended to millimeter-scale dimensions over multiterabyte data sets. This yields statistically large sample populations that can reveal subtle changes in the distributions of specific morphological parameters across different regions of the brain.

One such application involves the morphology of dendritic spines in different layers of the mouse cerebral cortex. A spine is a small (~ 0.01 to $1.0 \mu\text{m}^3$) membranous protrusion from a neuronal dendrite that receives synaptic input from the closely juxtaposed axon of another neuron. Spine morphology has been extensively studied with a variety of imaging methods (48),

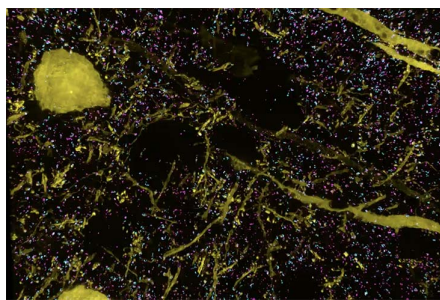
in part because it is related to synaptic strength (49), whose time- and activity-dependent change (plasticity) (50) is implicated in learning and memory consolidation (51). However, although optical methods such as Golgi impregnations (52), array tomography (6), and confocal (53) and two-photon microscopy (54, 55) can image the complete arborization of neurons spanning the cortex, they lack the 3D nanometric resolution needed to measure the detailed morphology of spines. Conversely, EM (56, 57) and SR fluorescence microscopy (58, 59) have the requisite resolution but not the speed to scale readily to cortical dimensions. ExLLSM, however, has both.

To demonstrate this, we imaged a 1900- by 280- by 70- μm tissue slice spanning the pia to the white matter in the primary somatosensory cortex of a transgenic Thy1-YFP mouse expressing cytosolic fluorescence within a sparse subset of layer V pyramidal neurons. The slice was additionally immunostained against Bassoon and Homer1 (Fig. 3A and Movie 4). In each of seven different regions across the cortex (Fig. 3B and fig. S13A), we selected four 27- by 27- by 14- μm subvolumes and used a modified commercial analysis pipeline (supplementary note

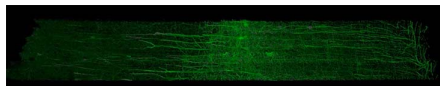
4f) (60) to segment (fig. S14 and movie S2) and measure spine ultrastructure. Across the ~ 1500 spines so measured, the range of spine head diameters, neck diameters, overall backbone lengths (spine root to tip), and neck backbone lengths (Fig. 3C and figs. S13B and S15) were consistent with those seen in an EM study of layer II/III pyramidal neurons in the mouse visual cortex (56). Furthermore, the absence of spines in the initial segment of the distal apical dendrite, and prevalence of much larger spines on smaller dendritic branches than on the remainder of the distal apical dendrite (Fig. 3D), were in line with an EM study of pyramidal neurons in the primary somatosensory cortex of the cat (61). Mean spine head diameter and mean neck backbone length each approximately doubled from layer II/III (position 1) to the regions of layers IV and V (positions 3 and 4) nearest the somata before falling again in layer VI (positions 6 and 7) to levels similar to layer II/III (table S4). This is consistent with a longitudinal *in vivo* study of spine morphology that found that spines closer to the soma, including those on proximal apical dendrites, were more mature and formed stronger synaptic connections than those on basal dendrites or the distal apical dendrite (62). We also found that head diameter and backbone length or neck backbone length were correlated across all layers of the cortex (Fig. 3C, top row; figs. S13B, top row, and S15; and table S4), but neck diameter and neck backbone length were not correlated across all regions (Fig. 3C, bottom row; fig. S13B, bottom row; and table S4).

Colabeling with Homer1-specific antibodies allowed us also to map excitatory synapses and their density (Fig. 3E) across the primary somatosensory cortex. In particular, when 4.5 million Homer1 puncta were binned in 50- by 50- by 25- μm subvolumes to average across local fluctuations, their density was revealed to be ~ 1.5 to $2.0 \times$ greater in layers II/III and V (~ 40 to 50 puncta/ μm^3) than in adjacent layers I, IV, and VI. Similar dual maxima in synaptic density are seen in sparsely sampled EM images of the rat somatosensory (63) and mouse barrel cortex (64), although in different cortical layers (rat, II and IV; mouse, I and IV) than seen in this work.

Focusing on the subset of Homer1 puncta colocalized with YFP-expressing dendritic spines, we found that thin spines were approximately twice as likely to coexpress Homer1 as spines classified as stubby, mushroom, or filopodial (fig. S16). As a synaptic scaffold protein, Homer1 plays an important role in the recruitment and cross-linking of other proteins that lead to the maturation and enlargement of spines (65–67), so Homer1's relative abundance at thin spines may presage their transformation to more mature forms. Surprisingly, we also observed dramatic variations in the expression of Homer1 within neighboring layer V pyramidal neurons: Homer1 was present at nearly all spines and throughout the cytosol of one neuron (Fig. 3D, neuron 1), whereas a parallel neuron $\sim 57 \mu\text{m}$ away of similar morphology exhibited very little Homer1,



Movie 3. Synaptic proteins and their associations to neuronal processes in layers IV and V of the mouse primary somatosensory cortex. Thy1-YFP-expressing neurons and immunostained pre- and postsynaptic proteins Bassoon and Homer1 across 75 by 100 by 125 μm , sequentially showing all Bassoon and Homer1 puncta, and only YFP-associated Bassoon and Homer1 pairs (Fig. 2, I to K, and fig. S12).



Movie 4. Relationship of postsynaptic Homer1 to neuronal processes across the mouse primary somatosensory cortex. Thy1-YFP-expressing neurons and immunostained postsynaptic protein Homer1 across 1900 by 280 by 70 μm in the primary somatosensory cortex, with specific focus on two adjacent layer V pyramidal neurons that exhibit substantially different patterns of Homer1 expression (Fig. 3, figs. S13 to S17, and movie S2).

even at its dendritic spines (Fig. 3D, neuron 2). This difference did not result from differential labeling efficiency because the density of Homer1 puncta in the immediate surrounds of each neuron was similar (fig. S17). Instead, because

Homer1 levels are known to change rapidly under different neuronal states [for example, asleep versus awake (68)], it may reflect the different excitatory states of these two neurons at the time the animal was sacrificed.

Visual cortex-spanning neuronal tracing and myelination patterns

Although the radial anisotropy of axonal myelination (Fig. 2E) can affect the speed and efficiency of AP propagation, so too can its

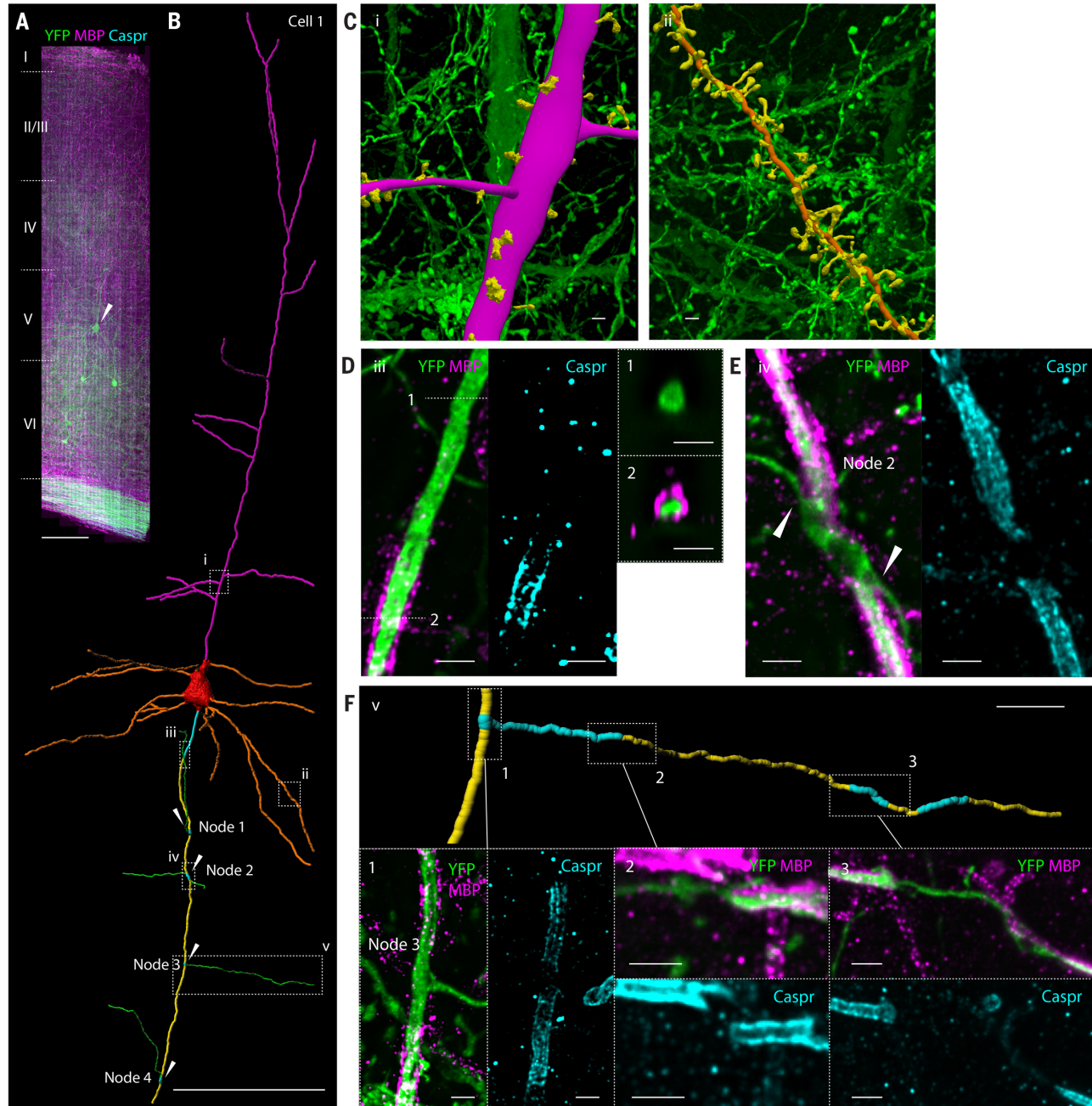


Fig. 4. Neural tracing and longitudinal myelination analysis across the mouse primary visual cortex. (A) Coronal MIP of a 25- μm -thick slab within a 1100- by 280- by 83- μm tissue section spanning the pia to the white matter of the primary visual cortex of a Thy1-YFP mouse (Movie 5), additionally immunostained against MBP and Caspr to highlight myelin sheaths and nodes of Ranvier, respectively. Scale bar, 100 μm . (B) Traced arborization (Movie 6) of a specific layer V pyramidal neuron denoted by the arrowhead in (A), showing the soma (red), apical (magenta), and basal (orange) dendrites; myelinated (yellow) and unmyelinated (cyan) axon segments; and collateral axon branches (green). Arrows indicate nodes of Ranvier. Scale bar, 100 μm . (C) Magnified segmented views of (left) the

distal apical dendrite and two of its branches and (right) a basal dendrite and its spines, from boxed regions i and ii in (B), respectively. Scale bars, 1 μm . (D) MIP view of boxed region iii in (B), showing (left) the distal end of the PMAS; (middle) Caspr at the start of myelination; and (right) cross-sectional views of the axon (1) before and (2) after the start of myelination. Scale bars, 1 μm . (E) MIP view of boxed region iv in (B), showing (left) break in myelination and two branching collateral axons at a node of Ranvier and (right) Caspr highlighting the two ends of the node. Scale bars, 1 μm . (F) (Top) Segmented view of a collateral axon with myelinated and unmyelinated sections from boxed region v in (B). (Bottom) Three MIP views of breaks in myelination with flanking Caspr. Scale bars, (top) 10 μm ; (bottom) 1 μm .

longitudinal variation. The repeated gaps in myelination at the nodes of Ranvier house ion channels that are essential to regenerate the AP during saltatory conduction (69), the hallmark of high-speed signal propagation in vertebrates. Recently, however, high-throughput EM imaging and axonal tracing at 30 by 30 by 240 nm/voxel (70) has revealed additional gaps in the axonal myelination of layer II/III neurons in the mouse primary visual cortex much larger (for example, 55 μm) than either the ~2 μm typical of the nodes of Ranvier or the shorter and rarer gaps observed in layers III to VI of the primary somatosensory cortex.

To determine whether these differences are more reflective of the layer of origination of the axon or the functional role of the cortical region studied (the somatosensory versus the visual cortex), we imaged at 27 by 27 by 50 nm/voxel a ~280- by 1100- by 83- μm tissue section

from the primary visual cortex extending from the pia to the white matter of a Thy1-YFP mouse. The tissue was additionally immunostained against MBP and contactin-associated protein (Caspr) (71) to visualize myelin sheaths and their terminations, respectively (Fig. 4A and Movie 5). Although the dense global staining of EM makes long-range 3D tracing of small neurites challenging, expression of YFP in a sparse subset of layer V and layer VI pyramidal neurons (72) enabled rapid semiautomatic tracing (supplementary note 4h) of axons, their myelination, and the entire arborization of selected neurons across the tissue section (Fig. 4B and Movie 6). This included the distal apical dendrite and its branches (Fig. 4C, i), basal dendrites and their spines (Fig. 4C, ii), the premyelin axonal segment (PMAS) (Fig. 4D), the nodes of Ranvier (Fig. 4E), and collateral branches of the main axon originating at the nodes (Fig.

4F). All these features matched the known morphologies of layer V pyramidal neurons (73) and were recapitulated in a second neuron traced throughout the volume (Fig. 5A and Movie 6).

Given this assurance, we traced the axons and their longitudinal myelination patterns for 10 neurons in layer V and 11 more in layer VI (Fig. 5B). Within the imaged volume, all of the layer V axons in the primary visual cortex exhibited continuous myelination beyond the end of the PMAS, except for the expected small gaps at the nodes of Ranvier. This is consistent with the myelination pattern seen previously for layer III to VI axons in the primary somatosensory cortex (70). The range of PMAS lengths we measured for these neurons (28 to 41 μm , mean = $34.9 \pm 1.1 \mu\text{m}$) was also consistent with the range found in layers V and VI of the primary somatosensory cortex (25 to 40 μm , mean = $33.7 \pm 2.4 \mu\text{m}$). The internodal spacing of the

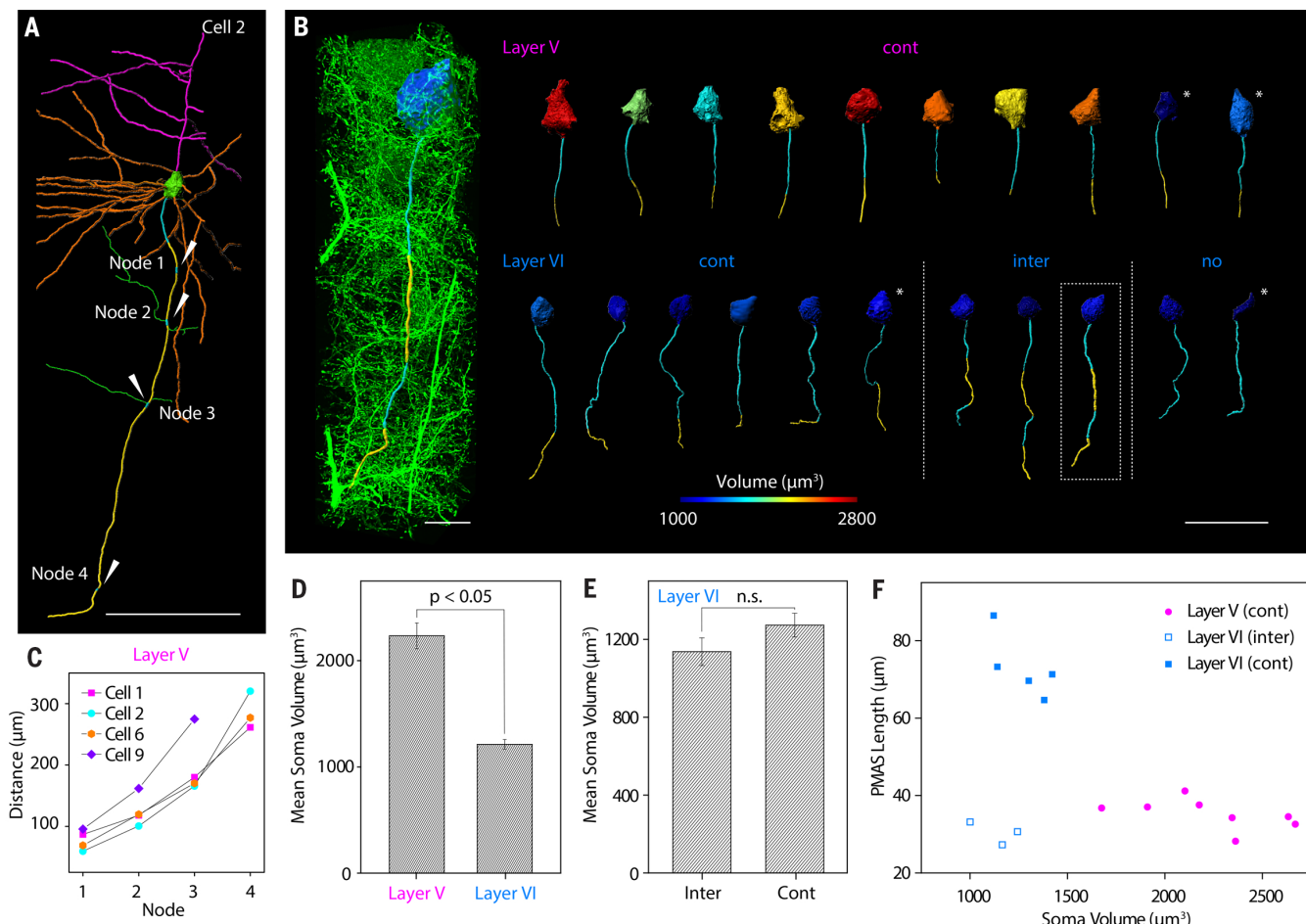


Fig. 5. Longitudinal myelination profiles of layer V and VI pyramidal neurons in the mouse primary visual cortex. (A) Traced arborization of a second layer V pyramidal neuron within the volume in Fig. 4A. Scale bar, 100 μm . (B) (Left) Segmented soma and axon of a pyramidal neuron shown in the context of its surroundings in layer VI. (Right) Segmented somata (color coded by volume) and axons, showing myelinated (yellow) and unmyelinated (cyan) segments, for 10 pyramidal neurons from layer V (top row) and 11 more from layer VI (bottom row). Boxed neuron is shown

at left. Scale bars, (left) 10 μm and (right) 50 μm . (C) Node spacing for four layer V neurons from (B) (fig. S18). (D) Volumes of eight layer V and nine layer VI somata fully within the image volume [no asterisks in (B)] (mean \pm SEM). (E) Volumes of the three somata with intermittently myelinated axons and five somata with continuously myelinated axons in layer VI (mean \pm SEM). The *P* values are calculated from a permutation test for medians. n.s., not significant. (F) Scatter plot of soma volume versus PMAS length for the neurons in (B) (fig. S19).

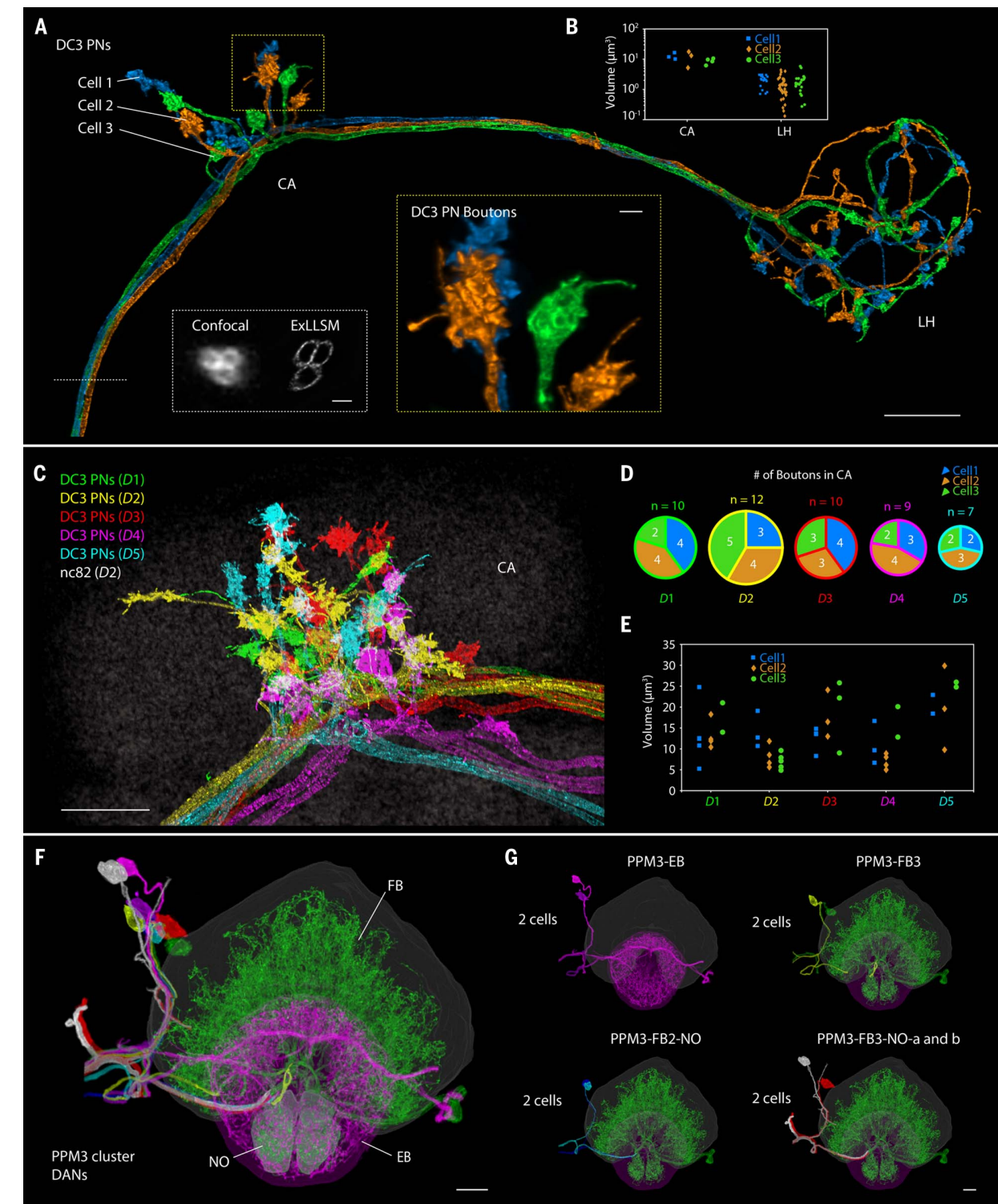


Fig. 6. Long-range tracing and stereotypy of neuron bundles in *Drosophila*. (A) MIP view of DC3 olfactory projection neurons (PNs) projecting from the antenna lobe of an adult *Drosophila* brain and partially traced here (Movie 7) to the calyx (CA) and lateral horn (LH). Scale bar, 10 μm . (Inset) (White box) Comparison of cross-sectional views of the axon bundle by means of (left) confocal microscopy and (right) ExLLSM. Scale bar, 1 μm . (Inset) (Yellow box) A magnified view of DC3 PN boutons in CA. Scale bar, 1 μm . (B) Volume of each individual DC3 PN bouton in CA and LH. (C) Overlaid MIP view of DC3 PNs from five adult *Drosophila*

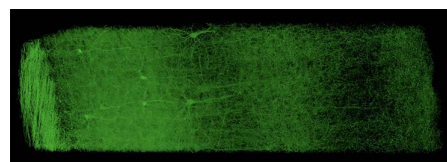
brains (D1 to D5) near CA. Scale bar, 10 μm . (D) Number of DC3 PN boutons in CA for D1 to D5 shown in (C). (E) Volume of DC3 PN boutons in CA for D1 to D5 shown in (C). (F) MIP view of individually traced PPM3 DANs in the right hemisphere of an adult *Drosophila* brain (Movie 8), innervating the fan-shaped body (FB) (green), ellipsoid body (EB) (magenta), and noduli (NO) (green). The fine neurites arborizing FB, EB, and NO are from both hemispheres of the brain. Scale bar, 10 μm . (G) MIP view of the identified cell types of PPM3 DANs (fig. S20). Scale bar, 10 μm .

four layer V neurons that could be traced to the white matter increased with increasing distance from the soma (Fig. 5C and fig. S18). By contrast, in layer VI only six axons were continuously myelinated, whereas two were completely unmyelinated, and three exhibited intermittent myelination with long unmyelinated segments more reminiscent of the layer II and III axons in the primary somatosensory cortex than the layer VI axons there (70). Thus, myelination patterns of axons in the primary visual cortex and the primary somatosensory cortex can differ, even for neurons in the same cortical layer.

Although the volumes of the somata and the diameters of the PMAS in layer V of the primary visual cortex were twice as large as those in layer VI (Fig. 5D and fig. S19, respectively), there was not a strong relationship between soma volume and myelination pattern (for example, intermittent or continuous) within layer VI (Fig. 5E). However, the PMAS lengths of the six continuously myelinated and the three intermittently myelinated axons in layer VI of the primary visual cortex split into distinct populations (Fig. 5F), with the intermittent ones of mean length ($30.3 \pm 1.7 \mu\text{m}$) similar to the axons of layer V, and the continuous ones more than twice as long ($70.6 \pm 3.6 \mu\text{m}$). Thus, continuously myelinated axons in different layers of the primary visual cortex need not have similar PMAS lengths. Given that the distal end of the PMAS is the site of AP initiation (74), perhaps PMAS length might be one mechanism by which neurons control the AP to account for differences in myelination or overall axon length in different layers and cortical regions.

Long-range tracing of clustered neurons in *Drosophila* and their stereotypy

Although millimeter-scale tissue sections present no problem for LLSM, the entire mouse brain is far too large, given the short working distances of commercially available high-resolution objectives. The brain of the fruitfly *D. melanogaster*, on the other hand, fits comfortably within the microscope, even in its 4 \times expanded form. Furthermore, a vast array of genetic tools have been developed for *Drosophila*, such as split-GAL4 drivers and MultiColor FlipOut (MCFO) (17), which enable precise labeling of user-



Movie 5. Neuronal processes and myelination patterns across the mouse primary visual cortex. Thy1-YFP-expressing neurons across 1100 by 280 by 83 μm , immunostained against myelin and Caspr, a marker of the nodes of Ranvier, with specific emphasis on the neuronal processes and longitudinal myelination profile of a selected layer V pyramidal neuron (Figs. 4 and 5 and figs. S18 and S19).

selected subsets of its ~100,000 neurons, such as the dorsal paired medial (DPM) neurons that innervate the mushroom bodies (MBs) (movie S3). Fluorescence imaging of thousands of such subsets across thousands of transgenic flies and collation of the results then yields brain-wide 3D reconstructions of complete neural networks at single-cell resolution (8, 9). However, to trace fine neuronal processes and identify synaptic connections, nanoscale resolution is needed. For all these reasons, the *Drosophila* brain is well matched to the capabilities of ExLLSM.

We thus chose to start with a relatively simple case: three olfactory projection neurons (PNs) originating at the DC3 glomerulus of the antennal lobes that feed most prominent sensory inputs to the calyx (CA) of the MB and lateral horn (LH) (75, 76). Imaging a ~250- by 175- by 125- μm volume, we were able to trace the axonal branches of all three DC3 PNs across one hemisphere (Fig. 6A and Movie 7), although tracing of fine dendritic processes was still difficult at 4 \times expansion. We were also able to precisely assign boutons to each cell within the CA (cell 1, 3 boutons; cell 2, 3 boutons; cell 3, 4 boutons) and the LH (cell 1, 19 boutons; cell 2, 32 boutons; cell 3, 23 boutons) and determine the shapes and sizes of the boutons in these regions (Fig. 6B).

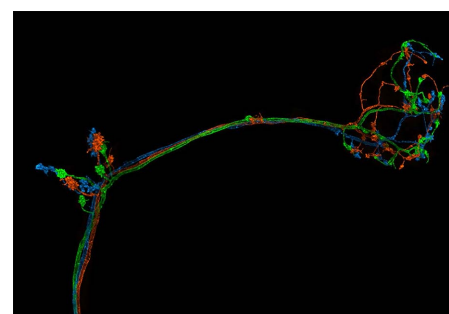
The neuronal circuits of the olfactory pathways to the MB have been extensively described by using light microscopy and have been re-

constructed completely in the L1 instar larva and partially in the adult brain by using EM (5, 77). However, the variation among individual animals has not been well studied at the level of detailed subcellular circuitry. The speed of ExLLSM now makes this possible. We studied the stereotypy of DC3 PNs by comparing their morphologies in the CA across five different animals (Fig. 6C). As expected, we consistently observed the restriction of boutons to the ends of the neurites in CA. However, we found that both the number and size of boutons differed among the three cells from the same hemisphere as well as between animals. For example, the total number of boutons in CA varied from 7 to 12, and none of the bouton assignments to each cell was the same among all five brains studied (Fig. 6D). The bouton size also showed substantial variability among the brains (Fig. 6E). These variations might arise from the distinct developmental histories of the individual animals. It is not yet clear whether they also indicate differences in synaptic strength and connection with Kenyon cells or how they might affect processing of olfactory information for associative learning in the MB. ExLLSM will enable such questions to be answered, thanks to its high throughput and its precise descriptions of neuronal morphology.

Given our success with this relatively simple example, we next applied ExLLSM to a much more challenging sample by imaging a ~340- by 660- by 90- μm volume covering nearly the entire brain of a TH-GAL4 transgenic *Drosophila* specimen. The sample was immunostained in one color against the membranes of all dopaminergic neurons (DANs) and in a second color with nc82 antibodies against Bruchpilot (Brp), a major structural and functional component of presynaptic active zones (AZs) (78, 79). Among the ~110 DANs within the image volume, we focused our efforts on tracing the protocerebral posterior medial 3 (PPM3) cluster of DANs that project to the central complex, a key brain region essential for navigation, visual memory, sleep, and aggression (80–82). With manual annotation, we identified and traced all eight



Movie 6. Segmentation of pyramidal neurons in layer V of the mouse primary visual cortex. Segmentation of two neurons, with specific emphasis on their branches and axonal myelination patterns (Fig. 4 and 5 and figs. S18 and S19).



Movie 7. Tracing of DC3 olfactory projection neurons (PNs) in an adult *Drosophila* brain. Volumetric view of three individually traced neurons projecting from the antenna lobe in a bundle, with magnified views of their boutons at the calyx and lateral horn (Fig. 6, A to E).

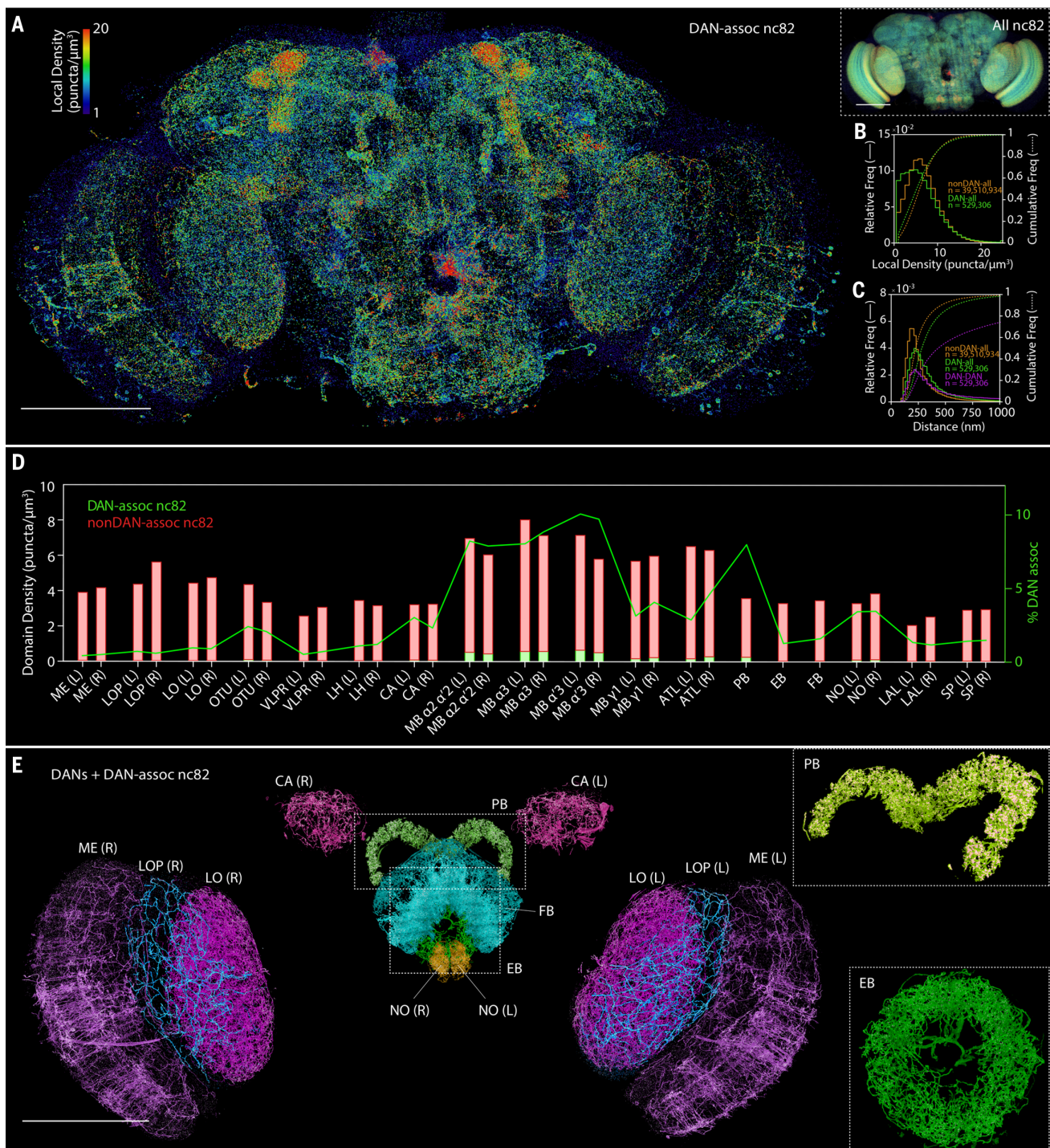


Fig. 7. Whole-brain analysis of presynaptic sites and DANs in *Drosophila*. (A) MIP view of the subset of nc82 puncta marking presynaptic sites that are associated with DANs (DAN-assoc nc82), color coded by the local puncta density, in an adult *Drosophila* brain (Movie 9). Scale bar, 100 μm . (Inset) (Right) MIP view of all nc82 puncta, using identical color coding of local density. Scale bar, 100 μm . (B) Distribution of local densities of (green) DAN-associated nc82 puncta and (orange) nonDAN-associated nc82 puncta in (A) (fig. S28). (C) Distribution of distances from DAN-associated nc82 puncta (green) and nonDAN-associated nc82 puncta (orange) to the nearest nc82 punctum of any kind, and nearest-neighbor distances from one DAN-associated nc82 to another (magenta) (fig. S29). (D) Volumetric density of DAN-associated nc82 puncta

(green bars) and nonDAN-associated nc82 puncta (red bars), and the percentage of nc82 puncta that are DAN-associated (green curve), within each of the 33 brain regions of the adult *Drosophila* brain (fig. S30). (E) MIP view of DANs and DAN-associated nc82 puncta, color coded by 13 representative brain region (Movie 10). Scale bar, 100 μm . (Insets) Magnified views of the (top, angled view) PB and (bottom) EB. Brain regions are ME, medulla; LOP, lobula plate; LO, lobula; OTU, optical tubercle; VLPR, ventrolateral protocerebrum; LH, lateral horn; CA, calyx; MB, mushroom body; ATL, antler; PB, protocerebral bridge; EB, ellipsoid body; FB, fan-shaped body; NO, noduli; LAL, lateral accessory lobe; and SP, superior protocerebrum. "L" and "R" indicate the left and right hemispheres of the brain, respectively.

individual cells within the cluster (Fig. 6F, figs. S20 and S21, Movie 8, table S5, and movie S4). Although tracing of fine processes inside the central complex was difficult, we were able to trace the main axonal branches and precisely determine the number of cell types and the number of cells belonging to each cell type. Within the PPM3 cluster, we found that two cells (PPM3-EB) mainly projected to the ellipsoid body (EB) (82); two cells (PPM3-FB3) projected to layer 3 of the fan-shaped body (FB); two cells (PPM3-FB2-NO) projected to layer 2 of the FB and noduli (NO); and two cells, which could be further categorized into two cell types (PPM3-FB3-NO-a and PPM3-FB3-NO-b), projected to layer 3 of the FB and NO (Fig. 6G, figs. S20 and S21, table S5, and supplementary note 6f). Using stochastic labeling of individual neurons and split-GAL4 intersection, we were able to identify and confirm the individual cell types we assigned (figs. S20 and S21, table S5, and supplementary note 6f).

Whole-brain analysis of presynaptic sites and DANs

We next turned our attention to the nc82 channel of this specimen because recent EM measurements of the nearest-neighbor distances between synapses in the α lobe of the MB (fig. S22) (83) suggest that quantitative counting of synapses across the *Drosophila* brain should be possible with ExLLSM at 4 \times expansion. However, to have confidence in the results, we needed to show that nc82 puncta larger than 100 nm represented true AZs and not nonfunctional Brp monomers or nonspecific background. To do so, we imaged two additional nc82-stained brains: one coimmunostained against V5-tagged Brp and the other coimmunostained against the AZ protein Syd1 (supplementary note 6c) (84, 85). In both cases, the distribution of distances from each nc82 punctum to its nearest

costained neighbor was consistent with their mutual incorporation in a single AZ (fig. S23). In addition, we imaged another brain sample of the output neuron from the $\alpha 1$ compartment of the MB (MBON- $\alpha 1$) to validate the specificity of nc82 antibody. We measured a 70-fold-higher surface density of nc82 puncta at the axons and boutons of MBON- $\alpha 1$ than at its dendrites (fig. S24 and supplementary note 6d), which is consistent with the near-absence of dendritic presynaptic densities observed for the same neuron with EM (83). Furthermore, we counted ~44,000 nc82 puncta in the $\alpha 3$ compartment (fig. S25), compared with ~34,000 presynaptic densities in the EM study (fig. S22 and supplementary note 6e). The distribution of distances between the presynaptic densities was also similar in the two cases (figs. S22B and S25B).

To see whether these differences were within typical specimen variability, we imaged three additional wild-type females and counted between ~34,000 and ~49,000 nc82 puncta in the $\alpha 3$ compartments of four MBs (fig. S26). Conversely, for the two animals in which we studied both $\alpha 3$ compartments (the original TH-GAL4 specimen and the wild type), the number of nc82 puncta in the left and right compartments were within ~10% of one another. This suggests that the variability we observed between animals, including the EM result, is indeed natural and not due to errors from our counting methodology.

Given confidence from these results, we then extended our analysis across nearly the entire brain (the medial lobes of the MB were not imaged because TH-GAL4 does not express in the DANs in that region). In total, we counted ~40 million nc82 puncta, ~530,000 of them localized at DANs (Fig. 7A and Movie 9), and calculated the brain-wide distribution of puncta density (Fig. 7B) and nearest-neighbor distances between any puncta or only DAN-associated ones (Fig. 7C).

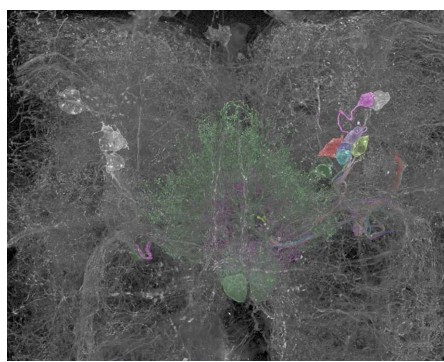
We observed substantial differences when we further subdivided our analysis into 33 major brain regions (fig. S28 to S30 and table S6). The volume density of all puncta, for example, varied from ~2 to 3 per cubic micrometer in the lateral accessory lobe (LAL) and superior protocerebrum (SP) to ~6 to 8 in the compartment-

ments of the MB (Fig. 7D), perhaps reflecting the distinct computational needs of different brain regions. The high density in the MB, for example, is likely beneficial for increasing capacity and sensory specificity of memory in associative learning.

When focusing on only those nc82 puncta associated with DANs, we found additional differences. For example, the distance between non-DAN nc82 puncta and DAN-associated nc82 puncta differed substantially between brain regions (fig. S29), indicating that the proportion of synapses that can be modulated by dopamine may differ between brain regions. We also found that the percentage of puncta associated with DANs was approximately 10-fold higher in the MB than in the optic lobes (Fig. 7D), which is consistent with dopamine-dependent heterosynaptic plasticity being the basis of associative learning in the MB (83, 86, 87). On the other hand, the FB and the EB, which are known for visual and place memory formation (88), exhibited surprisingly low DAN association, whereas the protocerebral bridge (PB) and the antler (ATL), which are not particularly known for heterosynaptic plasticity, showed high DAN association second only to the MB. Despite these differences, the variation in surface density of nc82 puncta on DANs in different brain regions was considerably less pronounced (fig. S30B) because the percentage volume occupied by DAN in each domain (fig. S30D) followed similar trends to the percentage of DAN-associated puncta (Fig. 7D). This could also be seen directly in volume renderings of the DANs and DAN-associated puncta in each brain region (Fig. 7E and Movie 10), although local intradomain variations in the spatial distribution of nc82 were also seen.

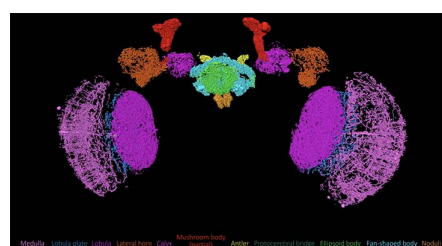
Discussion

Thanks to its combination of high imaging speed, low photobleaching rate, and 3D nanoscale resolution, ExLLSM extends, by at least 1000-fold in volume, the ability of SR fluorescence microscopy to generate detailed images of subcellular ultrastructure. This fills a valuable niche between the high throughput of conventional optical pipelines of neural anatomy

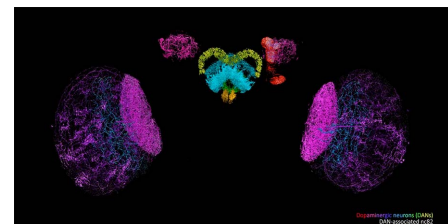


Movie 8. Tracing and classification of PPM3 dopaminergic neurons (DANs) in an adult *Drosophila* brain.

Drosophila brain. Section of brain near the central complex with eight neurons from the protocerebral posterior medial 3 (PPM3) cluster in the right hemisphere (colored) shown in relation to surrounding DANs (white), and tracing of the individual neurons to their paired innervations in different regions of the central complex (Fig. 6, F and G, and figs. S20 and S21).



Movie 9. Local density map of DAN-associated presynaptic sites across an adult *Drosophila* brain. Color-coded brain regions and 3D color-coded map of the local density of DAN-associated nc82 puncta in each domain (Fig. 7, A to D, and figs. S28 to S30).



Movie 10. DANs and DAN-associated presynaptic sites in different brain regions of an adult *Drosophila* brain. Volume rendered DANs, DAN-associated nc82 puncta, and all nc82 puncta across the entire brain, color coded by brain region, followed by magnified 3D and orthoslice views of DANs and DAN-associated nc82 in each of nine different domains (Fig. 7E).

(8, 9) and the ultrahigh resolution of corresponding EM pipelines (5, 70, 83). With genetically targeted cell type-specific labeling (17, 89–91) and protein-specific immunostaining, ExLLSM enables sparse neural subsets and dense synaptic connections to be recorded, visualized, and quantified at ~60- by 60- by 90-nm resolution with ~100 person-hours of effort over cortex-spanning volumes in the mouse or brain-wide volumes in *Drosophila*. This compares with 5 weeks to image and ~16,000 person-hours to trace all neurons and count all synapses in a volume only 1/80th of a fly brain encompassing the α lobe of the MB in a recent EM study at 8-nm isotropic resolution (83). The fluorescence contrast of ExLLSM also raises the possibility of correlating (92) fluorescence-based genetic indicators of neural activity (93, 94) with neural ultrastructure over much larger volumes and without the labeling compromises common to correlative EM/fluorescence studies (95).

Although we have focused on the mouse cortex and the *Drosophila* brain in this work, we have also applied ExLLSM to image the mossy fiber innervation of granule cells in glomeruli in the cerebellum of the mouse (fig. S31 and movie S5) as well as a complete human kidney glomerulus section (fig. S32). However, the application of ExM to any biological system must be examined on a case-by-case basis through careful controls and comparisons with known aspects (such as with EM) of the specific ultrastructural elements under investigation. In particular, extrapolating the faithful nanoscale expansion of delicate membranous structures and vesicles in a specimen from images of more robust components such as cytoskeletal elements, clathrin-coated pits, or nuclear histones (18, 29, 96, 97) should be avoided. Elastic inhomogeneity of the specimen after digestion, such as from collagen-rich connective tissue or adhesion to a rigid substrate, can also interfere with expansion, although newer protocols with more aggressive digestion may help (98). In this regard, brain tissue may represent a best case for ExM studies, owing to its comparatively homogenous mechanical properties and ready digestion. It should always be remembered that any image of a once-living specimen is an imperfect representation of that specimen, and the more steps that intrude in the process from one to the other the more imperfect it becomes. Overexpression, chemical fixation, permeabilization, and immunostaining already introduce numerous structural artifacts (99–101) in all forms of high-resolution fluorescence microscopy, including ExM, but ExM also requires additional steps of polymer infusion, gelation, label attachment, digestion, expansion, and handling that can perturb ultrastructure even more. Careful controls are essential.

At 4 \times expansion, the resolution of ExLLSM is close, but not quite sufficient, to trace fine, highly innervated neuronal processes—such as the PPM3 cluster, which terminates in the central complex—and would therefore benefit from higher expansion ratios. However, even if specimen-

wide isotropic expansion can be validated at higher ratios with newer protocols of iterated expansion (29), ExM is still heir to the problems that befall other forms of high-resolution fluorescence microscopy. Chief among these is that because of the stochastic nature of labeling, the mean separation between fluorophores must be ~5 \times to 10 \times smaller than the desired resolution in each dimension in order to distinguish with high confidence two or more structures for which no a priori knowledge exists (102). We met this requirement at the level of ~60- by 60- by 90-nm resolution in most cases owing to the dense expression of cytosolic label in Thy1-YFP transgenic mice and DAN membrane label in a TH-GAL4 transgenic fly, as well as the exceptional specificity of Abs targeting MBP and nc82. Other Abs in our study did not meet this standard but were sufficient to identify organelles responsible for voids of cytosolic label, mark Homer1 at synapses and Caspr at nodes of Ranvier, and measure statistical distributions of synapse breadth and pre- and post-synaptic separation. However, immunostaining in any form is probably not dense enough to achieve true 3D resolution much beyond that already obtainable at 4 \times expansion, and the long distance between epitope and fluorophore, particularly with secondary Abs, further limits resolution. Likewise, loss of FP fluorescence upon linking and digestion, as well as the slow continued loss of fluorescence, which we alleviated here with a highly basic imaging buffer (supplementary note 2, c and d), probably preclude study at high resolution of many FP-linked proteins at the endogenous levels produced through genome editing. Indeed, even at 4 \times expansion, we rarely found sufficient residual fluorescence to image targets labeled with red FPs of the Anthozoa family, despite reports to the contrary (19).

Despite these challenges and limitations, the high speed and nanometric 3D resolution of ExLLSM make it an attractive tool for comparative anatomical studies, particularly in the *Drosophila* brain. For example, although we imaged the entire TH-GAL4/nc82 brain in 62.5 hours ($3.2 \times 10^5 \mu\text{m}^3/\text{hour}$), with subsequent improvements in scanning geometry and field of view (FOV) we imaged mouse brain tissue in two colors at $4.0 \times 10^6 \mu\text{m}^3/\text{hour}$. If transferable to the fly, this would allow whole-brain imaging in ~5.0 hours. This limit is not fundamental; with simultaneous multicolor imaging and multiple cameras to cover even broader FOVs, rates up to $\sim 10^8 \mu\text{m}^3/\text{hour}$ may be achievable, or ~12 min/fly brain at 4 \times expansion. Assuming the future development of (i) robust, isotropic expansion at 10 \times or greater; (ii) longer working distance high NA water immersion objectives or lossless sectioning (103) of expanded samples; and (iii) a ubiquitous, dense, and cell-permeable fluorescent membrane stain analogous to heavy-metal stains in EM, even densely innervated circuits might be traced, particularly when imaged in conjunction with cell type-specific or stochastically expressed mul-

ticolor labels for error checking (104). With such a pipeline in place, 10 or more specimens might be imaged in a single day at 4 \times to 10 \times expansion, enabling statistically rich, brain-wide studies with protein-specific contrast and nanoscale resolution of neural development, sexual dimorphism, degree of stereotypy, and structure/function or structure/behavior correlations, particularly under genetic or pharmacological perturbation.

Materials and methods

Preparation of ExM samples

Mouse, *D. melanogaster*, and human samples were dissected, fixed, and immunostained following the protocols in supplementary note 1. Sample genotypes and antibodies are summarized in table S2. Unless otherwise noted, all samples were processed by using a protein-retention ExM (proExM) protocol with minor modifications (19, 105) or an expansion pathology (ExPath) protocol (98). Prepared ExM samples were stored in 1 \times phosphate-buffered saline at 4°C and expanded in doubly deionized water immediately before imaging with LLSM.

Lattice light-sheet imaging

With the exception of Fig. 1, all ExM samples were imaged in objective scan mode (20) by using a LLSM described previously (106), except with adaptive optics capability disabled. The ExM sample in the left column of Fig. 1 was imaged by using a LLSM optimized for ExM, featuring a broader 160- μm FOV, a 1.5-mm scan range, and software optimized for rapid sample scan acquisition (supplementary note 2a). All expanded samples were large compared with the LLS FOV and were therefore imaged in a series of overlapping 3D tiles that covered the desired sample volume (supplementary note 2b). For imaging sessions of several hours or more, focus was maintained through the periodic imaging of reference beads (supplementary note 2c). Raw data from each tile were deskewed (for sample scan mode), flat-fielded, deconvolved, and stored for subsequent processing.

Computing pipeline for flat-field correction, stitching, and export of 3D image tiles

Because automatic tools for 3D stitching (107–111) do not scale to datasets with thousands of 3D image tiles, we developed a scalable high-performance computing (HPC) pipeline to robustly flat-field correct, deconvolve, and assemble 3D image tiles into the final volume (supplementary note 3). First, we extended and parallelized CIDRE (107) for 3D volumes to calculate 3D flat fields (figs. S5 and S6). We then corrected the raw image tiles using these flat-fields and deconvolved each. Next, we parallelized the globally optimizing 3D stitching method (108) to automatically stitch the thousands of raw image tiles, without manual intervention, in an iteratively refined prediction model that corrects for systematic stage coordinate errors (fig. S7). Last, we exported the stitched datasets using the flat-field-corrected and deconvolved image tiles as multiresolution hierarchies

into a custom file format (N5) (21) that enabled parallel blockwise export and compression on a HPC cluster. Bindings for N5 format for the ImgLib2 library (112) are provided for the ImageJ distribution Fiji (113). For interactive visualization, we developed a BigDataViewer-based viewer plugin (114) including a crop and export tool to make arbitrary subvolumes available in legacy formats such as TIFF image series.

REFERENCES AND NOTES

- S. Herculano-Houzel, The human brain in numbers: A linearly scaled-up primate brain. *Front. Hum. Neurosci.* **3**, 31 (2009). doi: 10.3389/neuro.09.031.2009; pmid: 19915731
- K. Sharma et al., Cell type- and brain region-resolved mouse brain proteome. *Nat. Neurosci.* **18**, 1819–1831 (2015). doi: 10.1038/nn.4160; pmid: 26523646
- J. E. Heuser, T. S. Reese, Evidence for recycling of synaptic vesicle membrane during transmitter release at the frog neuromuscular junction. *J. Cell Biol.* **57**, 315–344 (1973). doi: 10.1083/jcb.57.2.315; pmid: 4348786
- C. S. Xu et al., Enhanced FIB-SEM systems for large-volume 3D imaging. *eLife* **6**, e25916 (2017). doi: 10.7554/eLife.25916; pmid: 28500755
- Z. Zheng et al., A complete electron microscopy volume of the brain of adult *Drosophila melanogaster*. *Cell* **174**, 730–743.e22 (2018). doi: 10.1016/j.cell.2018.06.019; pmid: 30033368
- K. D. Micheva, S. J. Smith, Array tomography: A new tool for imaging the molecular architecture and ultrastructure of neural circuits. *Neuron* **55**, 25–36 (2007). doi: 10.1016/j.neuron.2007.06.014; pmid: 17610815
- J.-C. Rah et al., Thalamocortical input onto layer 5 pyramidal neurons measured using quantitative large-scale array tomography. *Front. Neural Circuits* **7**, 177 (2013). doi: 10.3389/fncir.2013.00177; pmid: 24273494
- A. S. Chiang et al., Three-dimensional reconstruction of brain-wide wiring networks in *Drosophila* at single-cell resolution. *Curr. Biol.* **21**, 1–11 (2011). doi: 10.1016/j.cub.2010.11.056; pmid: 21129968
- A. Jenett et al., A GAL4-driver line resource for *Drosophila* neurobiology. *Cell Reports* **2**, 991–1001 (2012). doi: 10.1016/j.celrep.2012.09.011; pmid: 23063364
- M. N. Economo et al., A platform for brain-wide imaging and reconstruction of individual neurons. *eLife* **5**, e10566 (2016). doi: 10.7554/eLife.10566; pmid: 26796534
- S. Shah, E. Lubeck, W. Zhou, L. Cai, In situ transcription profiling of single cells reveals spatial organization of cells in the mouse hippocampus. *Neuron* **92**, 342–357 (2016). doi: 10.1016/j.neuron.2016.10.001; pmid: 27764670
- J. R. Moffitt et al., High-throughput single-cell gene-expression profiling with multiplexed error-robust fluorescence in situ hybridization. *Proc. Natl. Acad. Sci. U.S.A.* **113**, 11046–11051 (2016). doi: 10.1073/pnas.1612826113; pmid: 27625426
- J. Tønnesen, U. V. Nägerl, Superresolution imaging for neuroscience. *Exp. Neurol.* **242**, 33–40 (2013). doi: 10.1016/j.expneurol.2012.10.004; pmid: 23063602
- H. Zhong, Applying superresolution localization-based microscopy to neurons. *Synapse* **69**, 283–294 (2015). doi: 10.1002/syn.21806; pmid: 25648102
- C. I. Bargmann, Beyond the connectome: How neuromodulators shape neural circuits. *BioEssays* **34**, 458–465 (2012). doi: 10.1002/bies.201100185; pmid: 22396302
- J. Lu, J. C. Tapia, O. L. White, J. W. Lichtman, The intercervularis muscle connectome. *PLOS Biol.* **7**, e32 (2009). pmid: 19209956
- A. Nern, B. D. Pfeiffer, G. M. Rubin, Optimized tools for multicolor stochastic labeling reveal diverse stereotyped cell arrangements in the fly visual system. *Proc. Natl. Acad. Sci. U.S.A.* **112**, E2967–E2976 (2015). doi: 10.1073/pnas.1506763112; pmid: 25964354
- F. Chen, P. W. Tillberg, E. S. Boyden, Expansion microscopy. *Science* **347**, 543–548 (2015). doi: 10.1126/science.1260088; pmid: 25592419
- P. W. Tillberg et al., Protein-retention expansion microscopy of cells and tissues labeled using standard fluorescent proteins and antibodies. *Nat. Biotechnol.* **34**, 987–992 (2016). doi: 10.1038/nbt.3625; pmid: 27376584
- B. C. Chen et al., Lattice light-sheet microscopy: Imaging molecules to embryos at high spatiotemporal resolution. *Science* **346**, 1257998 (2014). doi: 10.1126/science.1257998; pmid: 25342811
- I. Pisarev, S. Saalfeld, Sticher and N5 viewer; <https://github.com/saalfeldlab/stitching-spark>, <https://github.com/saalfeldlab/n5-viewer>.
- J. Tønnesen, V. V. G. K. Inavalli, U. V. Nægerl, Super-resolution imaging of the extracellular space in living brain tissue. *Cell* **172**, 1108–1121.e15 (2018). doi: 10.1016/j.cell.2018.02.007; pmid: 29474910
- L. Freifeld et al., Expansion microscopy of zebrafish for neuroscience and developmental biology studies. *Proc. Natl. Acad. Sci. U.S.A.* **114**, E10799–E10808 (2017). doi: 10.1073/pnas.1706281114; pmid: 29162696
- T. J. Mosca, D. J. Luginbuhl, I. E. Wang, L. Luo, Presynaptic LRP4 promotes synapse number and function of excitatory CNS neurons. *eLife* **6**, e27347 (2017). doi: 10.7554/eLife.27347; pmid: 28606304
- C. K. Cahoon et al., Superresolution expansion microscopy reveals the three-dimensional organization of the *Drosophila* synaptosomal complex. *Proc. Natl. Acad. Sci. U.S.A.* **114**, E6857–E6866 (2017). doi: 10.1073/pnas.1705623114; pmid: 28760978
- A. Tsai et al., Nuclear microenvironments modulate transcription from low-affinity enhancers. *eLife* **6**, e28975 (2017). doi: 10.7554/eLife.28975; pmid: 29095143
- N. Jiang et al., Superresolution imaging of *Drosophila* tissues using expansion microscopy. *Mol. Biol. Cell* **29**, 1413–1421 (2018). doi: 10.1091/mbc.E17-10-0583; pmid: 29688792
- F. Guo, M. Holla, M. M. Diaz, M. Rosbash, A circadian output circuit controls sleep-wake arousal threshold in *Drosophila*. *bioRxiv* (2018). doi: 10.1101/298067
- J. B. Chang et al., Iterative expansion microscopy. *Nat. Methods* **14**, 593–599 (2017). doi: 10.1038/nmeth.4261; pmid: 28417997
- C. J. L. Sheppard, Super resolution in confocal imaging. *Optik (Stuttgart)* **80**, 53–54 (1988).
- C. B. Müller, J. Enderlein, Image scanning microscopy. *Phys. Rev. Lett.* **104**, 198101 (2010). doi: 10.1103/PhysRevLett.104.198101; pmid: 20867000
- X.-T. Cheng et al., Characterization of LAMP1-labeled nondegradative lysosomal and endocytic compartments in neurons. *J. Cell Biol.* **217**, 3127–3139 (2018). doi: 10.1083/jcb.201711083; pmid: 29695488
- N. Kasthuri et al., Saturated reconstruction of a volume of neocortex. *Cell* **162**, 648–661 (2015). doi: 10.1016/j.cell.2015.06.054; pmid: 26232230
- Q. A. Liu, H. Shio, Mitochondrial morphogenesis, dendrite development, and synapse formation in cerebellum require both Bcl-xL and the glutamate receptor 82. *PLOS Genet.* **4**, e1000097 (2008). doi: 10.1371/journal.pgen.1000097; pmid: 18551174
- V. Kuehnel, *Color Atlas of Cytology, Histology, and Microscopic Anatomy* (Thieme Flexibook, ed. 4, 2003).
- V. Popov, N. I. Medvedev, H. A. Davies, M. G. Stewart, Mitochondria form a filamentous reticular network in hippocampal dendrites but are present as discrete bodies in axons: A three-dimensional ultrastructural study. *J. Comp. Neurol.* **492**, 50–65 (2005). doi: 10.1002/cne.20682; pmid: 16175555
- M. R. Duchen, Mitochondria in health and disease: Perspectives on a new mitochondrial biology. *Mol. Aspects Med.* **25**, 365–451 (2004). doi: 10.1016/j.mam.2004.03.001; pmid: 15302203
- S. G. Waxman, M. V. I. Bennett, Relative conduction velocities of small myelinated and non-myelinated fibres in the central nervous system. *Nat. Rev. Biol.* **238**, 217–219 (1972). doi: 10.1038/nbio238217a0; pmid: 4506206
- K. A. Nave, Myelination and support of axonal integrity by glia. *Nature* **468**, 244–252 (2010). doi: 10.1038/nature09614; pmid: 21068833
- J. J. Harris, D. Attwell, The energetics of CNS white matter. *J. Neurosci.* **32**, 356–371 (2012). doi: 10.1523/JNEUROSCI.3430-11.2012; pmid: 22219296
- A. Compton, A. Coles, Multiple sclerosis. *Lancet* **372**, 1502–1517 (2008). doi: 10.1016/S0140-6736(08)61620-7; pmid: 18970977
- W. A. H. Rushton, A theory of the effects of fibre size in medullated nerve. *J. Physiol.* **115**, 101–122 (1951). doi: 10.1113/jphysiol.1951.sp004655; pmid: 14889433
- R. La Marca et al., TACE (ADAM17) inhibits Schwann cell myelination. *Nat. Neurosci.* **14**, 857–865 (2011). doi: 10.1038/nn.2849; pmid: 21666671
- L.-J. Oluich et al., Targeted ablation of oligodendrocytes induces axonal pathology independent of overt demyelination. *J. Neurosci.* **32**, 8317–8330 (2012). doi: 10.1523/JNEUROSCI.1053-12.2012; pmid: 22699912
- M. Zonouzi et al., GABAergic regulation of cerebellar NG2 cell development is altered in perinatal white matter injury. *Nat. Neurosci.* **18**, 674–682 (2015). doi: 10.1038/nn.3990; pmid: 25821912
- O. Oglebo, S. Cox, L. Humphreys, J. Burronne, Neuronal activity controls transsynaptic geometry. *Sci. Rep.* **6**, 22703 (2016). doi: 10.1038/srep22703; pmid: 26951792
- A. Dani, B. Huang, J. Bergan, C. Dulac, X. Zhuang, Superresolution imaging of chemical synapses in the brain. *Neuron* **68**, 843–856 (2010). doi: 10.1016/j.neuron.2010.11.021; pmid: 21144999
- N. L. Rochefort, A. Konnerth, Dendritic spines: From structure to in vivo function. *EMBO Rep.* **13**, 699–708 (2012). doi: 10.1038/embor.2012.102; pmid: 22791026
- H. Hering, M. Sheng, Dendritic spines: Structure, dynamics and regulation. *Nat. Rev. Neurosci.* **2**, 880–888 (2001). doi: 10.1038/35104061; pmid: 11733795
- E. A. Nimchinsky, B. L. Sabatini, K. Svoboda, Structure and function of dendritic spines. *Annu. Rev. Physiol.* **64**, 313–353 (2002). doi: 10.1146/annurev.physiol.64.081501.160008; pmid: 11826272
- M. Segal, Dendritic spines and long-term plasticity. *Nat. Rev. Neurosci.* **6**, 277–284 (2005). doi: 10.1038/nrn1649; pmid: 15803159
- S. Konur, D. Rabinowitz, V. L. Fenstermaker, R. Yuste, Systematic regulation of spine sizes and densities in pyramidal neurons. *J. Neurobiol.* **56**, 95–112 (2003). doi: 10.1002/neu.10229; pmid: 12838576
- D. Dumitriu, A. Rodriguez, J. H. Morrison, High-throughput, detailed, cell-specific neuroanatomy of dendritic spines using microinjection and confocal microscopy. *Nat. Protoc.* **6**, 1391–1411 (2011). doi: 10.1038/nprot.2011.389; pmid: 21886104
- M. Jiang et al., Dendritic arborization and spine dynamics are abnormal in the mouse model of MECP2 duplication syndrome. *J. Neurosci.* **33**, 19518–19533 (2013). doi: 10.1523/JNEUROSCI.1745-13.2013; pmid: 24336718
- X. Yu, Y. Zuo, Two-photon vivo imaging of dendritic spines in the mouse cortex using a thinned-skull preparation. *J. Vis. Exp.* **87**, e51520 (2014). pmid: 24894563
- J. I. Arellano, R. Benavides-Piccione, J. Defelipe, R. Yuste, Ultrastructure of dendritic spines: Correlation between synaptic and spine morphologies. *Front. Neurosci.* **1**, 131–143 (2007). doi: 10.3389/neuro.01.11.010.2007; pmid: 18982124
- C. Bosch et al., FIB/SEM technology and high-throughput 3D reconstruction of dendritic spines and synapses in GFP-labeled adult-generated neurons. *Front. Neuroanat.* **9**, 60 (2015). doi: 10.3389/fnana.2015.00060; pmid: 26052271
- K. Takasaki, B. L. Sabatini, Super-resolution 2-photon microscopy reveals that the morphology of each dendritic spine correlates with diffusive but not synaptic properties. *Front. Neuroanat.* **8**, 29 (2014). doi: 10.3389/fnana.2014.00029; pmid: 24847215
- J. Tønnesen, G. Katona, B. Rózsa, U. V. Nægerl, Spine neck plasticity regulates compartmentalization of synapses. *Nat. Neurosci.* **17**, 678–685 (2014). doi: 10.1038/nn.3682; pmid: 24657968
- D. L. Dickstein et al., Automatic dendritic spine quantification from confocal data with neurolucida 360. *Curr. Protoc. Neurosci.* **77**, 1, 21 (2016). doi: 10.1002/cpns.16; pmid: 27696360
- E. G. Jones, T. P. S. Powell, Morphological variations in the dendritic spines of the neocortex. *J. Cell Sci.* **5**, 509–529 (1969). pmid: 5362339
- J. Grutzendler, N. Kasthuri, W. B. Gan, Long-term dendritic spine stability in the adult cortex. *Nature* **420**, 812–816 (2002). doi: 10.1038/nature01276; pmid: 12490949
- L. Anton-Sánchez et al., Three-dimensional distribution of cortical synapses: A replicated point pattern-based analysis. *Front. Neuroanat.* **8**, 85 (2014). doi: 10.3389/fnana.2014.00085; pmid: 25206325
- J. DeFelipe, L. Alonso-Nanclares, J. I. Arellano, Microstructure of the neocortex: Comparative aspects. *J. Neurocytol.* **31**, 299–316 (2002). doi: 10.1023/A:102413021265; pmid: 12815249
- C. Sala et al., Regulation of dendritic spine morphology and synaptic function by Shank and Homer. *Neuron* **31**, 115–130 (2001). doi: 10.1016/S0896-6273(01)00339-7; pmid: 11498055

66. U. Thomas, Modulation of synaptic signalling complexes by Homer proteins. *J. Neurochem.* **81**, 407–413 (2002). doi: [10.1046/j.jn.1417-4159.2002.00869.x](https://doi.org/10.1046/j.jn.1417-4159.2002.00869.x); pmid: [21206549](#)
67. A. Dosemeci, R. J. Weinberg, T. S. Reese, J.-H. Tao-Cheng, The postsynaptic density: There is more than meets the eye. *Front. Synaptic Neurosci.* **8**, 23 (2016). doi: [10.3389/fnsyn.2016.00023](https://doi.org/10.3389/fnsyn.2016.00023); pmid: [27594834](#)
68. G. H. Diering et al., Homer1a drives homeostatic scaling-down of excitatory synapses during sleep. *Science* **355**, 511–515 (2017). doi: [10.1126/science.aai8355](https://doi.org/10.1126/science.aai8355); pmid: [28154077](#)
69. D. Debanne, E. Campanac, A. Bialowas, E. Carlier, G. Alcaraz, Axon physiology. *Physiol. Rev.* **91**, 555–602 (2011). doi: [10.1152/physrev.00048.2009](https://doi.org/10.1152/physrev.00048.2009); pmid: [21527732](#)
70. G. S. Tomassy et al., Distinct profiles of myelin distribution along single axons of pyramidal neurons in the neocortex. *Science* **344**, 319–324 (2014). doi: [10.1126/science.1249766](https://doi.org/10.1126/science.1249766); pmid: [24744380](#)
71. S. Einheber et al., The axonal membrane protein Caspr, a homologue of neurexin IV, is a component of the septate-like paranodal junctions that assemble during myelination. *J. Cell Biol.* **139**, 1495–1506 (1997). doi: [10.1083/jcb.139.6.1495](https://doi.org/10.1083/jcb.139.6.1495); pmid: [9396755](#)
72. C. Porrero, P. Rubio-Garrido, C. Avendaño, F. Clascá, Mapping of fluorescent protein-expressing neurons and axon pathways in adult and developing Thy1-YFP-H transgenic mice. *Brain Res.* **1345**, 59–72 (2010). doi: [10.1016/j.brainres.2010.05.061](https://doi.org/10.1016/j.brainres.2010.05.061); pmid: [20510892](#)
73. S. Ramaswamy, H. Markram, Anatomy and physiology of the thick-tufted layer 5 pyramidal neuron. *Front. Cell. Neurosci.* **9**, 233 (2015). doi: [10.3389/fncel.2015.00233](https://doi.org/10.3389/fncel.2015.00233); pmid: [26167146](#)
74. L. M. Palmer, G. J. Stuart, Site of action potential initiation in layer 5 pyramidal neurons. *J. Neurosci.* **26**, 1854–1863 (2006). doi: [10.1523/JNEUROSCI.4812-05.2006](https://doi.org/10.1523/JNEUROSCI.4812-05.2006); pmid: [16467534](#)
75. S. J. C. Caron, V. Ruta, L. F. Abbott, R. Axel, Random convergence of olfactory inputs in the *Drosophila* mushroom body. *Nature* **497**, 113–117 (2013). doi: [10.1038/nature12063](https://doi.org/10.1038/nature12063); pmid: [23615618](#)
76. N. J. Butcher, A. B. Friedrich, Z. Lu, H. Tanimoto, I. A. Meinertzhagen, Different classes of input and output neurons reveal new features in microglomeruli of the adult *Drosophila* mushroom body calyx. *J. Comp. Neurol.* **520**, 2185–2201 (2012). doi: [10.1002/cne.23037](https://doi.org/10.1002/cne.23037); pmid: [22237598](#)
77. K. Eichler et al., The complete connectome of a learning and memory centre in an insect brain. *Nature* **548**, 175–182 (2017). doi: [10.1038/nature23455](https://doi.org/10.1038/nature23455); pmid: [28796202](#)
78. W. Fouquet et al., Maturation of active zone assembly by *Drosophila* Bruchpilot. *J. Cell Biol.* **186**, 129–145 (2009). doi: [10.1083/jcb.200812150](https://doi.org/10.1083/jcb.200812150); pmid: [19596851](#)
79. N. Ehmann et al., Quantitative super-resolution imaging of Bruchpilot distinguishes active zone states. *Nat. Commun.* **5**, 4650 (2014). doi: [10.1038/ncomms5650](https://doi.org/10.1038/ncomms5650); pmid: [25130366](#)
80. Z. Mao, R. L. Davis, Eight different types of dopaminergic neurons innervate the *Drosophila* mushroom body neuropil: Anatomical and physiological heterogeneity. *Front. Neural Circuits* **3**, 5 (2009). doi: [10.3389/neuro.04.005.2009](https://doi.org/10.3389/neuro.04.005.2009); pmid: [19597562](#)
81. E. C. Kong et al., A pair of dopamine neurons target the D1-like dopamine receptor DopR in the central complex to promote ethanol-stimulated locomotion in *Drosophila*. *PLOS ONE* **5**, e9954 (2010). doi: [10.1371/journal.pone.0009954](https://doi.org/10.1371/journal.pone.0009954); pmid: [20376353](#)
82. O. V. Alekseyenko et al., Single serotonergic neurons that modulate aggression in *Drosophila*. *Curr. Biol.* **24**, 2700–2707 (2014). doi: [10.1016/j.cub.2014.09.051](https://doi.org/10.1016/j.cub.2014.09.051); pmid: [25447998](#)
83. S. Y. Takemura et al., A connectome of learning and memory center in the adult *Drosophila* brain. *eLife* **6**, e26975 (2017). doi: [10.7554/eLife.26975](https://doi.org/10.7554/eLife.26975); pmid: [28718765](#)
84. D. Owald et al., A Syd-1 homologue regulates pre- and postsynaptic maturation in *Drosophila*. *J. Cell Biol.* **188**, 565–579 (2010). doi: [10.1083/jcb.200908055](https://doi.org/10.1083/jcb.200908055); pmid: [20176924](#)
85. S. Holbrook, J. K. Finley, E. L. Lyons, T. G. Herman, Loss of syd-1 from R7 neurons disrupts two distinct phases of presynaptic development. *J. Neurosci.* **32**, 18101–18111 (2012). doi: [10.1523/JNEUROSCI.1350-12.2012](https://doi.org/10.1523/JNEUROSCI.1350-12.2012); pmid: [23238725](#)
86. Y. Aso et al., The neuronal architecture of the mushroom body provides a logic for associative learning. *eLife* **3**, e04577 (2014). doi: [10.7554/eLife.04577](https://doi.org/10.7554/eLife.04577); pmid: [25535793](#)
87. Y. Aso, G. M. Rubin, Dopaminergic neurons write and update memories with cell-type-specific rules. *eLife* **5**, e16135 (2016). doi: [10.7554/eLife.16135](https://doi.org/10.7554/eLife.16135); pmid: [27441388](#)
88. L. Kahsai, T. Zars, Learning and memory in *Drosophila*: Behavior, genetics, and neural systems. *Int. Rev. Neurobiol.* **99**, 139–167 (2011). doi: [10.1016/B978-0-12-387003-2.00006-9](https://doi.org/10.1016/B978-0-12-387003-2.00006-9); pmid: [21906539](#)
89. H. Luan, N. C. Peabody, C. R. Vinson, B. H. White, Refined spatial manipulation of neuronal function by combinatorial restriction of transgene expression. *Neuron* **52**, 425–436 (2006). doi: [10.1016/j.neuron.2006.08.028](https://doi.org/10.1016/j.neuron.2006.08.028); pmid: [17088209](#)
90. B. D. Pfeiffer et al., Refinement of tools for targeted gene expression in *Drosophila*. *Genetics* **186**, 735–755 (2010). doi: [10.1534/genetics.110.119917](https://doi.org/10.1534/genetics.110.119917); pmid: [20697123](#)
91. M. J. Dolan et al., Facilitating neuron-specific genetic manipulations in *Drosophila melanogaster* using a split GAL4 repressor. *Genetics* **206**, 775–784 (2017). doi: [10.1534/genetics.116.199687](https://doi.org/10.1534/genetics.116.199687); pmid: [28363977](#)
92. D. D. Bock et al., Network anatomy and in vivo physiology of visual cortical neurons. *Nature* **471**, 177–182 (2011). doi: [10.1038/nature09802](https://doi.org/10.1038/nature09802); pmid: [21390124](#)
93. T.-W. Chen et al., Ultrasensitive fluorescent proteins for imaging neuronal activity. *Nature* **499**, 295–300 (2013). doi: [10.1038/nature12354](https://doi.org/10.1038/nature12354); pmid: [2386258](#)
94. B. F. Fosque et al., Neural circuits. Labeling of active neural circuits in vivo with designed calcium integrators. *Science* **347**, 755–760 (2015). doi: [10.1126/science.1260922](https://doi.org/10.1126/science.1260922); pmid: [25678659](#)
95. P. de Boer, J. P. Hoogenboom, B. N. G. Giepmans, Correlated light and electron microscopy: Ultrastructure lights up! *Nat. Methods* **12**, 503–513 (2015). doi: [10.1038/nmeth.3400](https://doi.org/10.1038/nmeth.3400); pmid: [26020503](#)
96. T. J. Chozinski et al., Expansion microscopy with conventional antibodies and fluorescent proteins. *Nat. Methods* **13**, 485–488 (2016). doi: [10.1038/nmeth.3833](https://doi.org/10.1038/nmeth.3833); pmid: [27064647](#)
97. T. Ku et al., Multiplexed and scalable super-resolution imaging of three-dimensional protein localization in size-adjustable tissues. *Nat. Biotechnol.* **34**, 973–981 (2016). doi: [10.1038/nbt.3641](https://doi.org/10.1038/nbt.3641); pmid: [27454740](#)
98. Y. Zhao et al., Nanoscale imaging of clinical specimens using pathology-optimized expansion microscopy. *Nat. Biotechnol.* **35**, 757–764 (2017). doi: [10.1038/nbt.3892](https://doi.org/10.1038/nbt.3892); pmid: [28714966](#)
99. U. Schnell, F. Dijk, K. A. Sjollema, B. N. G. Giepmans, Immunolabeling artifacts and the need for live-cell imaging. *Nat. Methods* **9**, 152–158 (2012). doi: [10.1038/nmeth.1855](https://doi.org/10.1038/nmeth.1855); pmid: [22290187](#)
100. D. R. Whelan, T. D. M. Bell, Image artifacts in single molecule localization microscopy: Why optimization of sample preparation protocols matter. *Sci. Rep.* **5**, 7924 (2015). doi: [10.1038/srep07924](https://doi.org/10.1038/srep07924); pmid: [25603780](#)
101. D. Li et al., ADVANCED IMAGING. Extended-resolution structured illumination imaging of endocytic and cytoskeletal dynamics. *Science* **349**, aab3500 (2015). doi: [10.1126/science.aab3500](https://doi.org/10.1126/science.aab3500); pmid: [26315442](#)
102. W. R. Legant et al., High-density three-dimensional localization microscopy across large volumes. *Nat. Methods* **13**, 359–365 (2016). doi: [10.1038/nmeth.3797](https://doi.org/10.1038/nmeth.3797); pmid: [26590745](#)
103. K. J. Hayworth et al., Ultrastructurally smooth thick partitioning and volume stitching for large-scale connectomics. *Nat. Methods* **12**, 319–322 (2015). doi: [10.1038/nmeth.3292](https://doi.org/10.1038/nmeth.3292); pmid: [25686390](#)
104. Y.-G. Yoon et al., Feasibility of 3D reconstruction of neural morphology using expansion microscopy and barcode-guided agglomeration. *Front. Comput. Neurosci.* **11**, 97 (2017). doi: [10.3389/fncom.2017.00097](https://doi.org/10.3389/fncom.2017.00097); pmid: [29114215](#)
105. S. M. Asano et al., Expansion microscopy: Protocols for imaging proteins and RNA in cells and tissues. *Curr. Protoc. Cell Biol.* **80**, e56 (2018). doi: [10.1002/cpbc.56](https://doi.org/10.1002/cpbc.56); pmid: [30070431](#)
106. T. L. Liu et al., Observing the cell in its native state: Imaging subcellular dynamics in multicellular organisms. *Science* **360**, eaao1392 (2018). doi: [10.1126/science.aao1392](https://doi.org/10.1126/science.aao1392); pmid: [29674564](#)
107. K. Smith et al., CIDRE: An illumination-correction method for optical microscopy. *Nat. Methods* **12**, 404–406 (2015). doi: [10.1038/nmeth.3323](https://doi.org/10.1038/nmeth.3323); pmid: [25775044](#)
108. S. Preibisch, S. Saalfeld, P. Tomancak, Globally optimal stitching of tiled 3D microscopic image acquisitions. *Bioinformatics* **25**, 1463–1465 (2009). doi: [10.1093/bioinformatics/btp184](https://doi.org/10.1093/bioinformatics/btp184); pmid: [19346324](#)
109. D. Hörl et al., BigStitcher: Reconstructing high-resolution image datasets of cleared and expanded samples. *bioRxiv* (2018). doi: [10.1101/343954](https://doi.org/10.1101/343954)
110. M. Emmenauer et al., XuIVTools: Free, fast and reliable stitching of large 3D datasets. *J. Microsc.* **233**, 42–60 (2009). doi: [10.1111/j.1365-2818.2008.03094.x](https://doi.org/10.1111/j.1365-2818.2008.03094.x); pmid: [19196411](#)
111. A. Bria, G. Iannello, TeraStitcher—A tool for fast automatic 3D-stitching of teravoxel-sized microscopy images. *BMC Bioinformatics* **13**, 316 (2012). doi: [10.1186/1471-2105-13-316](https://doi.org/10.1186/1471-2105-13-316); pmid: [23181553](#)
112. T. Pietzsch, S. Preibisch, P. Tomancák, S. Saalfeld, ImgLib2—Generic image processing in Java. *Bioinformatics* **28**, 3009–3011 (2012). doi: [10.1093/bioinformatics/bts543](https://doi.org/10.1093/bioinformatics/bts543); pmid: [22962343](#)
113. J. Schindelin et al., Fiji: An open-source platform for biological-image analysis. *Nat. Methods* **9**, 676–682 (2012). doi: [10.1038/nmeth.2019](https://doi.org/10.1038/nmeth.2019); pmid: [22743772](#)
114. T. Pietzsch, S. Saalfeld, S. Preibisch, P. Tomancák, BigDataViewer: Visualization and processing for large image data sets. *Nat. Methods* **12**, 481–483 (2015). doi: [10.1038/nmeth.3392](https://doi.org/10.1038/nmeth.3392); pmid: [26020499](#)

ACKNOWLEDGMENTS

We thank D. Bock, K. Svoboda, N. Ji, N. Spruston, L. Scheffer, E. Snapp, P. Tillberg, L. Lavis, E. Bloss, W. Legant, D. Hoffman, and K. Hayworth at Howard Hughes Medical Institute (HHMI) Janelia Research Campus (JRC) and B. Sabatini and D. Van Vactor at Harvard Medical School (HMS) for invaluable discussions and comments. We also thank K. Schaefer, T. Wolff, C.-L. Chang, and H. Choi at JRC for help with sample preparation and imaging. We gratefully acknowledge the shared resources and project teams at JRC, including D. Alcor, J. Heddleston, and A. Taylor of the Advanced Imaging Center and Light Microscopy Facility for help with imaging; I. Negashov and jET for manufacturing expertise; and O. Malkesman, K. Salvesen, C. Christoforou, G. Meissner, and the FlyLight project team for sample handling and preparation. Last, we are grateful to C. Pama and R. Karadottir at the University of Cambridge; J. Melander and H. Zhong at OHSU; T. Herman at the University of Oregon; and E. Karagiannis, J.-S. Kang, and F. Chen at MIT for help with sample preparation and H. Otsuna, T. Kawase, and E. Bas at JRC; C. Wietholt at FEI Amira; M. Gastinger at Bitplane; and J. McMullen and T. Treadwell at MBF Bioscience for data analysis and visualization. **Funding:** I.P., D.E.M., T.-L.L., V.S., A.G., J.B., C.M.O., J.L.-S., A.H., G.M.R., S.S., Y.A., and E.B. are funded by HHMI. E.S.B. acknowledges, for funding, John Doerr, the Open Philanthropy Project, NIH 1R01NS087950, NIH 1RM1HG008525, NIH 1R01DA045549, NIH 2R01DA029639, NIH 1R01NS102727, NIH 1R41MH112318, NIH 1R01EB024261, NIH 1R01MH110932, the HHMI-Simons Faculty Scholars Program, IARPA D16PC00008, U.S. Army Research Laboratory and the U.S. Army Research Office under contract/grant W911NF1510548, U.S.–Israel Binational Science Foundation Grant 2014509, and NIH Director’s Pioneer Award 1DP1NS087724. S.U. and T.K. are funded by grants from Biogen, Ionis Pharmaceuticals, and NIH grant R01GM075252 (to T.K.). S.U. gratefully acknowledges the Fellows program of the Image and Data Analysis Core at Harvard Medical School and the MATLAB code repository received from the Computational Image Analysis Workshop, supported by NIH grant GM103792. K.R.M. and S.G.M. are funded by NIH grant R01DC015478. S.T. and A.R. are funded by NIH grant R44MH093011. **Author contributions:** E.B., E.S.B., and R.G. supervised the project and wrote the manuscript with input from all coauthors. T.-L.L. and J.C. built the microscopes with input from E.B., D.E.M., and jET (JRC) and performed all microscope characterization experiments. D.E.M. created the instrument control software. R.G., S.M.A., T.-L.L., V.S., J.C., and C.M.O. acquired all biological data with coauthors. G.H.H. provided the Thy1-YFP mice, and R.G. and S.M.A. prepared the ExM samples. A.G. and A.H. provided the Slc17a7-cre X TCGO mice and prepared the ExM samples. Y.Z. provided the human kidney sections and prepared the ExPath samples. Y.A. and G.M.R. created the split-GAL4 fly strains, Y.A. optimized the IHC conditions, and R.G. and S.M.A. prepared the ExM samples. K.R.M., S.G.M., S.M.A., and T.-L.L. provided the initial stitching software packages. I.P. and S.S. created the automated flat-field, stitching, and N5 visualization pipeline, and I.P., R.G., J.B., and S.S. deconvolved, flat-fielded, and stitched all image data. Y.A. performed segmentation and tracing and supervised analyses of all fly image data. C.Z., S.T., and A.R. provided customized commercial software packages and helped with segmentation, tracing and reconstruction of neurites and dendritic spines using these packages. S.-H.S. and H.A.P. designed experimental protocols and performed sample preparation for FIB-SEM. S.P., C.S.X., and H.H. performed FIB-SEM sample preparation, image acquisition, and data processing. J.L.-S. and T.K. provided essential discussion on the subcellular ultrastructure analysis and access to instrumentation and computational resources. S.U. and R.G. processed and performed quantitative analysis of all image data. S.U., R.G., E.B., and Y.A. produced all figures and

movies. **Competing interests:** Portions of the technology described here are covered by U.S. patent 7,894,136 issued to E.B., assigned to Lattice Light of Ashburn, VA, and licensed to Carl Zeiss Microscopy; U.S. patents 8,711,211 and 9,477,074 issued to E.B., assigned to HHMI, and licensed to Carl Zeiss Microscopy; U.S. patent application 13/844,405 filed by E.B. and assigned to HHMI; and U.S. patent 9,500,846 issued to E.B. and assigned to HHMI. E.S.B. is a co-inventor on multiple patents related to ExM and is also a cofounder of a company that aims to provide kits and services relating to ExM to the public. R.G. is a co-inventor on multiple patents related to ExM. Y.Z. is a co-inventor on multiple

patents related to ExM. **Data and materials availability:** All data needed to evaluate the conclusions in the paper are present in the paper or the supplementary materials. The compressed size of the datasets used in generating the figures and movies exceeds 100 terabytes, and it is therefore not practical to upload to a public data repository. All data used in this paper will be made freely available to those who request and provide a mechanism for feasible data transfers (such as physical hard disk drives or cloud storage). Documentation for construction of a LLSM can be obtained by execution of a research license agreement with HHMI.

SUPPLEMENTARY MATERIALS

www.sciencemag.org/content/363/6424/eau8302/suppl/DC1
Supplementary Text
Figs. S1 to S33
Table S1 to S6
References (115–133)
Movies S1 to S7

19 July 2018; accepted 30 November 2018
10.1126/science.aau8302

Cortical column and whole-brain imaging with molecular contrast and nanoscale resolution

Ruixuan Gao, Shoh M. Asano, Srigokul Upadhyayula, Igor Pisarev, Daniel E. Milkie, Tsung-Li Liu, Ved Singh, Austin Graves, Grace H. Huynh, Yongxin Zhao, John Bogovic, Jennifer Colonell, Carolyn M. Ott, Christopher Zugates, Susan Tappan, Alfredo Rodriguez, Kishore R. Mosaliganti, Shu-Hsien Sheu, H. Amalia Pasolli, Song Pang, C. Shan Xu, Sean G. Megason, Harald Hess, Jennifer Lippincott-Schwartz, Adam Hantman, Gerald M. Rubin, Tom Kirchhausen, Stephan Saalfeld, Yoshinori Aso, Edward S. Boyden and Eric Betzig

Science 363 (6424), eaau8302.
DOI: 10.1126/science.aau8302

Combining expansion and the lattice light sheet

Optical and electron microscopy have made tremendous inroads into understanding the complexity of the brain. Gao *et al.* introduce an approach for high-resolution tracing of neurons, their subassemblies, and their molecular constituents over large volumes. They applied their method, which combines expansion microscopy and lattice light-sheet microscopy, to the mouse cortical column and the entire *Drosophila* brain. The approach can be performed at speeds that should enable high-throughput comparative studies of neural development, circuit stereotypy, and structural correlations to neural activity or behavior.

Science, this issue p. eaau8302

ARTICLE TOOLS

<http://science.sciencemag.org/content/363/6424/eaau8302>

SUPPLEMENTARY MATERIALS

<http://science.sciencemag.org/content/suppl/2019/01/16/363.6424.eaau8302.DC1>

REFERENCES

This article cites 129 articles, 33 of which you can access for free
<http://science.sciencemag.org/content/363/6424/eaau8302#BIBL>

PERMISSIONS

<http://www.sciencemag.org/help/reprints-and-permissions>

Use of this article is subject to the [Terms of Service](#)